PHYSICAL REVIEW E **93**, 043203 (2016)

Ionic transport in high-energy-density matter

Liam G. Stanton[1,*] and Michael S. Murillo[2,*]
[1]*Center for Applied Scientific Computing, Lawrence Livermore National Laboratory, Livermore, California 94550, USA*
[2]*Computational Physics and Methods Group, MS D413, Los Alamos National Laboratory, Los Alamos, New Mexico 87545, USA*

(Received 16 November 2015; published 8 April 2016)

Ionic transport coefficients for dense plasmas have been numerically computed using an effective Boltzmann approach. We have developed a simplified effective potential approach that yields accurate fits for all of the relevant cross sections and collision integrals. Our results have been validated with molecular-dynamics simulations for self-diffusion, interdiffusion, viscosity, and thermal conductivity. Molecular dynamics has also been used to examine the underlying assumptions of the Boltzmann approach through a categorization of behaviors of the velocity autocorrelation function in the Yukawa phase diagram. Using a velocity-dependent screening model, we examine the role of dynamical screening in transport. Implications of these results for Coulomb logarithm approaches are discussed.

DOI: 10.1103/PhysRevE.93.043203

I. INTRODUCTION

Coulomb collisional processes in plasmas occur in many scenarios, ranging from particle and energy transport (e.g., self-diffusion, interdiffusion, thermal diffusion, viscosity, thermal conduction, stopping power, temperature relaxation, and electrical conduction) to wave damping, particulate drag, wake formation, and others. Central to the description of such processes is the Coulomb logarithm (CL), which is usually defined as

$$\ln \Lambda = \ln\left(\frac{b_{\max}}{b_{\min}}\right). \tag{1}$$

Here $b_{\max}$ and $b_{\min}$ are the maximum and minimum impact parameters, respectively. These parameters arise through truncating both limits in an integral [see, e.g., (5) below] over the impact parameter of the form $\int db/b$; these integrals would otherwise be divergent. The importance of knowing the correct CL cannot be overestimated, as the CL is used in a variety of applications, including numerical methods, such as direct-simulation Monte Carlo [1], multilevel Monte Carlo [2], particle-in-cell [3], and continuous-time Monte Carlo [4] methods, and modeling of physical systems, including stellar envelopes [5], dusty plasmas [6], ultracold plasmas [7,8], inertial confinement fusion (ICF) [9–14], laser ablation [15], and star clusters [16], among other physical systems.

Typically, $b_{\max}$ is chosen to be a screening length λ and $b_{\min}$ is chosen to be the distance of closest approach $\mathcal{D} \approx Z_1 Z_2 e^2/T$, where $Z_i e$ is the ionic charge and T is the temperature in energy units. The need to supply these two parameters can be traced to two independent approximations. In the binary scattering description of the Boltzmann equation, the relevant integrated cross sections for the Coulomb interaction are divergent owing to the long-range nature of the Coulomb potential. This divergence as $b \to \infty$ is attenuated by introducing many-body screening into $b_{\max}$ *ex post facto*. That is, the Boltzmann equation, or any more approximate kinetic equation obtained from it, requires the use of an effective potential between charged particles. Such many-body screening in Coulomb systems was first described by Debye and Hückel [17] in the context of electrolytes and was generalized by Pines and Bohm [18] in the context of the dynamical properties of dense electron gases. However, the Boltzmann formulation does allow for an impact parameter of $b = 0$; thus, no $b_{\min}$ cutoff is needed and strong scattering is well described. In the weak-scattering limit of the Boltzmann equation, one obtains the Landau (Fokker-Planck) equation [19], which introduces an additional divergence at $b = 0$, thereby requiring the $b_{\min}$ cutoff. This divergence is handled by noting that the strength of scattering is bounded by trajectories at the distance of closest approach $\mathcal{D}$. The Landau approach thereby includes strong scattering, again *ex post facto*. Today, we understand this situation in the context of kinetic theory, as illustrated in Fig. 1. The Boltzmann branch, which contains the Landau equation as a subset, is the binary scattering approximation of the full Bogoliubov-Born-Green-Kirkwood-Yvon (BBGKY) hierarchy [20,21] and, for this reason, requires an effective potential to handle Coulomb systems. The choices $b_{\max}$ and $b_{\min}$ in (1) implicitly reflect some choice of effective potential.

Alternatively, kinetic equations can be obtained via a correlation expansion that innately includes screening; that is, the effective potential arises naturally. Significant conceptual progress was made by Lenard [22] and Balescu [23] through their development of such a parallel branch of kinetic theory (parallel to that of Boltzmann), yielding two complementary approaches, as shown in Fig. 1. In Lenard-Balescu (LB) approaches, many-body effects arise naturally through a dynamical dielectric response [18] that gives rise to an effective potential of the form $v(k)/\epsilon(k,\omega)$ and thus a $b_{\max}$ need not be specified; however, because the correlation expansion is perturbative, a $b_{\min}$ divergence remains for classical systems [24].

A sense of the importance of these issues can be seen by choosing λ to be the classical Debye-Hückel (DH) screening length $\lambda_{\rm DH} = \sqrt{T/4\pi n Z^2 e^2}$ and noting that $\ln \Lambda \approx \ln(1/\sqrt{3}\Gamma^{3/2})$, where $\Gamma = Z^2 e^2/aT$ is the Coulomb coupling parameter in terms of the ion-sphere radius $a = (3/4\pi n)^{1/3}$, where n is the number density; the CL becomes negative when $\Gamma > 3^{-1/3}$ (≈ 0.7), suggesting that CL-based models fail significantly near and above this value. Because of

---

[*] liam@llnl.gov, murillo@lanl.gov

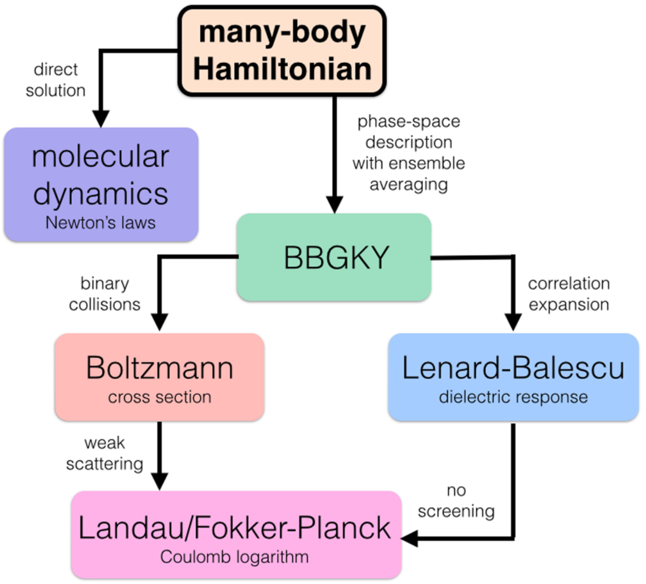

FIG. 1. Relevant structure of kinetic theory. From a many-body Hamiltonian, one solves the equations of motion either directly, as in molecular dynamics, or through an approximation of the BBGKY hierarchy [20,21]. Most approximations made in the latter case are of two types, either binary-collision approximations, which handle strong collisions well using a cross section, or correlation expansions, which include many-body physics only in the weak-scattering limit. Here we aim to exploit both avenues via the use of an effective potential, motivated by the right (Lenard-Balescu) branch, in a numerical cross section from the left (Boltzmann) branch. Finally, this approach is compared with the Landau (weak, binary-scattering) approach, which uses a so-called Coulomb logarithm.

the challenge of directly measuring collisional processes in high-energy-density experiments in this coupling regime, researchers have turned to comparisons with the results of molecular-dynamics (MD) codes incorporating higher-fidelity physics; in such codes, the trajectories of particles in many-body systems are computed directly [25–27]. This approach is shown in the top branch of Fig. 1.

Given the structure of kinetic theory [21] shown in Fig. 1 and the limitations of the two complementary branches, a fully convergent kinetic theory (CKT), which provides a self-consistent treatment of both strong scattering and screening without any adjustable parameters, is desired. In the seminal work of Liboff [28], the Chapman-Enskog (CE) solution of the Boltzmann equation with an effective potential was analyzed to find effective CLs that include strong scattering and screening while allowing the full integration over impact parameters (that is, $b_{\min} = 0$ and $b_{\max} = \infty$). Nearly simultaneously, Kihara [29] also emphasized the importance of directly including potentials of mean force [30–33] to describe irreversible transport processes in binary-scattering calculations rather than a more naive choice for the effective potential. Aono [34] extended these ideas to include both strong scattering and *dynamical* screening, thereby yielding a convergent result that improves upon the static screening assumptions of Liboff and Kihara and is more consistent with predictions of the LB approach. We now understand that the approaches of Liboff, Kihara, and Aono are combinations of the two branches in Fig. 1 that include properties of the Boltzmann equation at a small impact parameter and the LB equation at a large impact parameter, and these works laid the groundwork for more formal theoretical developments by Frieman and Book [35], Kihara and Aono [36], and Gould and DeWitt [37], all of which combine aspects of the Boltzmann and LB branches.

More recent developments in Coulomb collisional processes in the spirit of CKT have been proposed by Brown *et al.* [38], whose findings are in good agreement with MD results [25]. None of these works, however, are applicable across coupling regimes. A seminal contribution, in the context of stellar-evolution modeling, was that of Muchmore [39], who both numerically computed cross sections with an effective potential and proposed a coupling correction in the screening length, which will be discussed in detail below. This particular model was then numerically explored and tabulated by Paquette, Pelletier, Fontaine, and Michaud (PPFM) [5]. In a different, but similar, treatment of the screening length in the context of temperature relaxation, Gericke, Murillo, and Schlanges (GMS) [9,40] proposed an effective CL that included strong-coupling corrections in the effective screening length used in $b_{\max}$; comparisons with MD simulations [25,26] revealed the accuracy of such an effective-potential approach across coupling regimes, and this model will also be discussed in more detail below. The models of Muchmore, PPFM, and GMS are all based on choosing an optimal effective screening length in a Yukawa-like effective potential. Such approaches have recently been extended by Grabowski *et al.* [27] to the dynamical process of charged-particle stopping across coupling regimes, using a hypernetted-chain approach that directly computes the effective potential and yields excellent agreement with nonequilibrium MD simulations as well.

In parallel with these CKT developments, the Landau (Fokker-Planck) approach was extended by many authors, including Chandrasekhar [41], Cohen *et al.* [42], and Rosenbluth *et al.* [43], and in all of these approaches, the doubly divergent form was retained (1). More recently, in the context of ICF, Li and Petrasso [13] have derived the leading-order (inverse CL) corrections to the Fokker-Planck equation and have applied these corrections to stopping power [14]; however, while yielding a correction to the Fokker-Planck equation, the basic CL is unmodified and remains an input parameter. In contrast with these Boltzmann-based approaches, additional, recent results have built upon the LB branch. Strong scattering (associated with $b_{\min}$) and coupling are incorporated in these approaches with local field corrections; Ichimaru and co-workers [44,45] have developed CKTs based on such an approach. In related work, an effective CL for the one-component plasma valid across coupling regimes has been proposed by Khrapak [46]; this CL is based on a modification of the effective $b_{\min}$ that accounts for regions of negative density in the DH theory.

In this work we build upon these recent results by first constructing effective potentials, as suggested in the works of Kihara, Muchmore, GMS, and Grabowski *et al.*, and we compute ionic transport coefficients using a CE approach similar to those of Liboff and Muchmore. The paper is structured as follows. In Sec. II we introduce the Boltzmann formalism [5,27,39,40] in the CE [47] expansion to assess the importance of treating the cross section directly. In addition, we review the pathologies associated with neglecting many-body effects in a bare Coulomb collision. The concept of an effective potential is introduced in Sec. III, in which the many-body problem is cast as an effective two-body problem. We then numerically compute cross sections and collision integrals in Sec. IV and present simple, accurate fits to the calculations. These results are compared with various formulations of the CL to reveal the relative importance of specific approximations made in the CL derivation. In Sec. V we explore the implications of our results for several transport coefficients in the context of various phenomena; we include in this section a validation of our results with MD and several results for self-diffusion. Because our results are based on an effective Boltzmann equation, we explore the validity of the binary collision approximation in Sec. VI by examining transitions between different behaviors of the velocity autocorrelation function. We additionally explore the role of dynamical screening on transport in this section using a velocity-dependent screening model. Finally, concluding remarks are presented in Sec. VII.

II. COULOMB LOGARITHM

In a plasma, the bare interaction between two particles with charges $Z_i e$ and $Z_j e$, respectively, is given by the Coulomb potential ($4\pi\varepsilon_0 = 1$)

$$u_{ij}(r) = \frac{Z_i Z_j e^2}{r}. \tag{2}$$

Here the charges are either the bare nuclear charge or the mean ionization state; see Appendix A for a more detailed discussion. For the remainder of this work, we use atomic units such that $e = \hbar = m_e = 1$; however, these variables will occasionally be used to provide context. The resulting scattering angle of a collision can be calculated as

$$\theta_{ij}(b,v) = \pi - 2b\int_{r_0}^{\infty} \frac{dr}{r^2\sqrt{1-\left(\frac{b}{r}\right)^2 - \frac{2}{\mu_{ij}v^2}u_{ij}(r)}}, \tag{3}$$

where b is the impact parameter of the collision, v is the relative velocity between the particles, and the reduced mass is given by $\mu_{ij} = m_i m_j/(m_i + m_j)$, with m_k being the mass of the kth particle. The lower limit of integration r_0 is the distance of closest approach, which is the largest root of the equation

$$1 - \left(\frac{b}{r_0}\right)^2 - \frac{2}{\mu_{ij}v^2}u_{ij}(r_0) = 0. \tag{4}$$

The scattering angle can in turn be used to calculate the momentum-transfer cross sections

$$\sigma_{ij}^{(n)}(v) = 2\pi\int_0^{\infty} db\, b\{1 - \cos^n[\theta_{ij}(b,v)]\}. \tag{5}$$

For first-order CE theory, only the values $n = \{1,2\}$ are needed. Finally, the relevant collision integrals are given by

$$\Omega_{ij}^{(n,m)} = \left(\frac{T}{2\pi\mu_{ij}}\right)^{1/2}\int_0^{\infty} dV e^{-V^2} V^{2m+3}\sigma_{ij}^{(n)}(V), \tag{6}$$

$$V^2 = \frac{\mu_{ij}v^2}{2T}, \quad m = \{1,2,3\}. \tag{7}$$

A discussion of how (6) is used in transport models is given in Appendix B. For the remainder of this work, the subscripts i and j will be omitted unless required to distinguish between interactions between different types of species. Using (3), the relevant scattering angle of a binary (Coulomb) collision is then

$$\theta_C(b,v) = 2\sin^{-1}\left(\frac{1}{\sqrt{1+\epsilon^2 b^2}}\right), \quad \epsilon = \frac{\mu v^2}{Z_i Z_j e^2}. \tag{8}$$

If we then use (8) to calculate the momentum-transfer cross section, we encounter a divergence as $b \to \infty$ in (5). If this upper limit is instead truncated at some $b_{\max} = \lambda$, the integration of (5) gives finite cross sections

$$\sigma_C^{(1)}(v) = \left(\frac{4\pi}{\epsilon^2}\right)\frac{1}{2}\ln(1+\epsilon^2\lambda^2), \tag{9}$$

$$\sigma_C^{(2)}(v) = \left(\frac{4\pi}{\epsilon^2}\right)\left[\ln(1+\epsilon^2\lambda^2) + \frac{\epsilon^2\lambda^2}{1+\epsilon^2\lambda^2}\right]. \tag{10}$$

Note that no notion of $b_{\min}$ is required to bound this calculation. Before moving on, we should understand what this approximation means physically. It should be emphasized that introducing a truncated range in the impact parameter is *not equivalent* to truncating the range of the Coulomb interaction. As shown in Fig. 2, all particles with a sufficiently small impact parameter will interact throughout their *entire* trajectories, while the remaining particles will never interact with each other.

If one were instead to approximate the system with a truncated-Coulomb (TC) interaction, where $u_{ij}(r) = (Z_i Z_j e^2)/r$ for $r < \lambda$ and $u_{ij}(r) = 0$ otherwise, the scattering angle would then take the form

$$\theta_{\rm TC} = 2\cos^{-1}\left(\frac{(1+2w^2)\rho}{\sqrt{1+4(1+w^2)w^2\rho^2}}\right), \tag{11}$$

$$\rho = \frac{b}{\lambda}, \quad w^2 = \frac{\mu_{ij}\lambda v^2}{2Z_i Z_j e^2}. \tag{12}$$

For all impact parameters with $\rho > 1$, the angle is not defined and should be taken as zero, because there is no interaction in this range. Note that Eq. (3) cannot be used to calculate this angle, as it assumes a continuous interaction over all distances. The corresponding momentum-transfer cross section can also be calculated as

$$\sigma_{\rm TC}^{(1)} = 2\pi\lambda^2\left[\frac{\ln[1+4(1+w^2)w^2]}{4(1+w^2)w^2}\right]. \tag{13}$$

A similar expression can be obtained for $\sigma_{\rm TC}^{(2)}$ but has been omitted for brevity. We have plotted $\sigma_{\rm TC}^{(1)}/2\pi\lambda^2$ as a function of the dimensionless velocity w in Fig. 3 and compared it to the corresponding Coulomb interaction in (9). While qualitatively similar, the behaviors of the cross sections differ at intermediate values of w.

Before Eq. (6) is used to calculate the collision integrals for binary Coulomb interactions, it is common to make two *additional* approximations. First, the explicit velocity dependence of the logarithms in (9) is usually neglected and

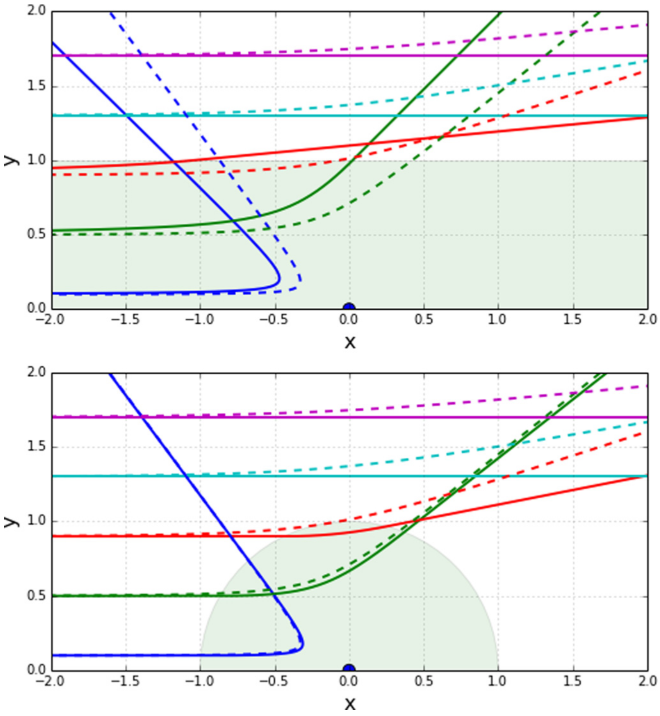

FIG. 2. Collision trajectories for various impact parameters in the reference frame of one of the particles placed at the origin. All lengths are in units of the screening length and all trajectories are for the same fixed initial energy of $E = 4Z^2e^2/\lambda$. In both panels, the dashed line indicates the trajectory for a full Yukawa potential. In the top panel, the solid lines are trajectories computed by assuming a pure Coulomb potential *everywhere* for particles that enter with impact parameters below unity (in these dimensionless units), as indicted by the green region, while particles not entering in this range of impact parameters experience no force *anywhere*. In the bottom panel, the impact parameter cutoff is replaced by a distance cutoff (below the screening length), as indicated by a circular green region, and a potential of zero elsewhere; this is the TC model described in the text. Each of the three trajectory types yields different scattering angles, with some improvement offered by the TC model over the more common impact parameter cutoff model.

replaced by some thermal velocity

$$\sigma^{(1)}_{\text{th}}(v) = \left(\frac{4\pi}{\epsilon^2}\right) \ln \Lambda_{\text{hyp}}, \tag{14}$$

$$\ln \Lambda_{\text{hyp}} \equiv \frac{1}{2} \ln \left[1 + \left(\frac{2T\lambda}{Z_i Z_j e^2} \right)^2 \right]. \tag{15}$$

Next, weak coupling is also assumed in the argument of the logarithm to yield

$$\sigma^{(1)}_{\text{WC}}(v) = \left(\frac{4\pi}{\epsilon^2}\right) \ln \Lambda, \quad \ln \Lambda \equiv \ln \left(\frac{2T\lambda}{Z_i Z_j e^2} \right). \tag{16}$$

Here both (14) and (16) contain CLs. The latter CL in (16) is in the form of (1), where $b_{\max} = \lambda$ and $b_{\min} = Z_i Z_j e^2/2T$, which can be negative for certain parameters. As the CL in (14) still contains some information about the hyperbolic trajectories of the collisions (rather than straight-line trajectories), positivity of the logarithm is maintained. Either form results in the following simple expression for the first-order collision integral:

$$\Omega^{(11)} = \frac{\sqrt{\pi} Z_i^2 Z_j^2 e^4}{2\sqrt{2\mu T^3}} \ln \Lambda; \tag{17}$$

however, each CL can introduce spurious and even pathological physics into the model. As already mentioned, the weak-coupling approximation in (16) can yield negative cross sections and thus negative collision integrals for sufficiently large values of the plasma parameter $g = Z_i Z_j e^2/\lambda T$ such that $g > 2$. Second, the thermal approximation in (14), while always positive, lacks a velocity dependence in the logarithmic term that cannot be approximated with a constant value in the collision integrals even for $g \ll 1$. To illustrate this issue, we have calculated $\Omega^{(11)}_{ij}$ using both the velocity-dependent cross section in (9) and the thermally approximated cross section in (14) and have then plotted the ratio of these two quantities as a function of g in Fig. 4. It can be seen that the thermal approximation is a *singular* perturbation of the collision integral and thus there is a significant deviation from the true result for any finite g.

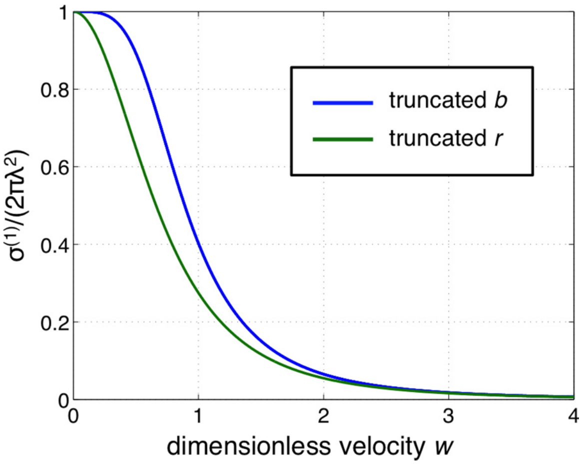

FIG. 3. Reduced cross section $\sigma^{(1)}/2\pi\lambda^2$ as a function of the dimensionless velocity $w = (\mu\lambda/2Z_iZ_je^2)^{1/2}v$ for truncated Coulomb interactions (green lower curve) and Coulomb interactions using the truncated impact parameter $b_{\max} = \lambda$ (blue upper curve). While the two interactions result in qualitatively similar cross sections, these cross sections differ for moderate values of w.

To summarize this section, the derivation of the CL (from a Boltzmann perspective) requires a series of uncontrolled approximations; our numerical results will shed light on their applicability.

III. EFFECTIVE POTENTIALS IN PLASMAS

As mentioned in Sec. I, no notion of $b_{\min}$ is needed in (1) within a Boltzmann description (i.e., $b_{\min} = 0$); however, $b_{\max}$ is still required to bound the cross sections. The presence of $b_{\max}$ and its connection to screening reveal that transport in plasmas is inherently a many-body process. Rather than generalize the Boltzmann equation by including many-body collisions directly with higher-order correlation functions [48,49], it is far more practical to cast the many-body problem

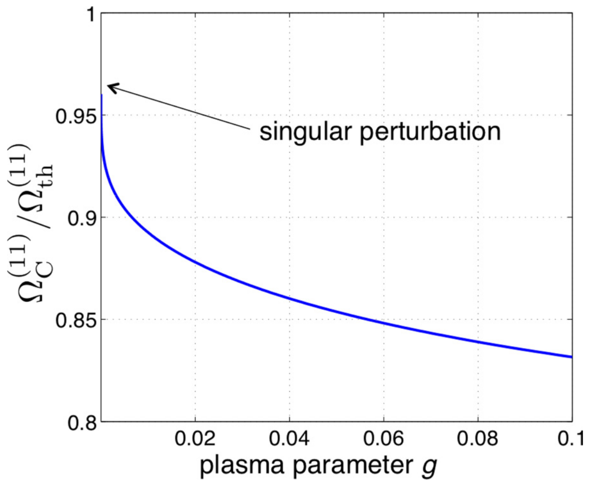

FIG. 4. Ratio of the collision integral $\Omega_C^{(11)}$ (velocity-dependent CL), calculated using (9), to the collision integral $\Omega_{\rm th}^{(11)}$ (velocity-independent CL), calculated using (14), as a function of the plasma parameter $g = Z_i Z_j e^2/\lambda T$. The thermal-velocity approximation within the CL is a singular perturbation and thus approaches the Coulomb form logarithmically as $g \to 0$. This illustrates the magnitude of the error that results from neglecting the full velocity dependence of the cross section.

in terms of an *effective* two-body problem, which in turn allows (3)–(6) to be used. This effective Boltzmann (EB) approach, which was developed by Liboff [28], Kihara [29], and Aono [34], has the additional advantage of including contributions from the *full* density. At the lowest order, the presence of a screening length can be rigorously incorporated through an effective pair potential described by the so-called screened Coulomb (SC) (or Yukawa) interaction

$$u_{\rm eff}(r) = \frac{Z_i Z_j e^2}{r} e^{-r/\lambda}, \tag{18}$$

where λ is the screening length. While (18) is obviously an approximation, it still represents the leading-order behavior of a screened interaction and in the most important plasma regimes of weak to moderate coupling, this form is likely to be accurate. The SC potential has several additional benefits. First, we wish to determine which screening length to use in the Boltzmann context and it is crucial that this length be well defined, as it is in the SC model. Second, such a choice allows all of the numerical results of this work to be presented, discussed, and fit to a single functional form, with the choice of λ left to the context in which the results will be used.

In our present work we will additionally assume a plasma with ions being linearly screened by background electrons (or any background species) and hence the pair interaction between two particles is given by

$$u_{ij}(r) = \frac{Z_i Z_j e^2}{r} e^{-r/\lambda_e}. \tag{19}$$

Here the electron screening length λ_e is not to be confused with the screening length in (18), which would include the screening effects from ions as well. For example, it is (19) that would be used in MD or Monte Carlo simulations, where the ionic screening would be included through the many-body calculation. Furthermore, Eq. (19) can be thought of as the first-order generalization of a pure Coulomb system, which is lacking in any screening from background electrons, and the results for this special case can be obtained by simply letting $\lambda_e \to \infty$. However, plasmas in which electron screening is negligible are rare in nature.

A. Effective screening length

The choice of the screening length λ is crucial to accurately encode the many-body physics lacking in binary collision models and there are many potential choices. For ionic collisions, an intuitive choice is the electron screening length, or $\lambda = \lambda_e$. However, to construct an effective potential that includes the surrounding medium, a better choice might be the total screening length

$$\lambda = \lambda_{\rm tot} = \left(\frac{1}{\lambda_e^2} + \frac{1}{\lambda_{\rm ion}^2}\right)^{-1/2}, \tag{20}$$

which includes both electrons and ions. In high-energy-density (HED) environments, specific choices for these lengths are the DH theory for N ionic species

$$\lambda_i = \left(\frac{T}{4\pi Z_i^2 e^2 n_i}\right)^{1/2}, \tag{21}$$

$$\lambda_{\rm ion} = \left(\sum_{i=1}^{N} \frac{1}{\lambda_i^2}\right)^{-1/2}, \tag{22}$$

where n_i is the number density of the ith ionic species, and the (nonrelativistic) Thomas-Fermi (TF) length for the electrons

$$\lambda_e^{-2} \approx \lambda_{\rm TF}^{-2} = \frac{\sqrt{8T}}{\pi} \mathcal{F}_{-1/2}(\beta\mu_e), \tag{23}$$

where the electron chemical potential μ_e is related to the electron density n_e through

$$n_e = \sum_{i=1}^{N} Z_i n_i = \frac{\sqrt{2T^3}}{\pi^2} \mathcal{F}_{1/2}(\beta\mu_e) \tag{24}$$

and $\beta = 1/T$ is the inverse temperature (in energy units). The TF screening length naturally includes degeneracy and recovers the electron DH screening length $\lambda_e \sim (4\pi e^2 n_e/T)^{-1/2}$ in the appropriate limits. Here the Fermi-Dirac integral of order p is defined as $\mathcal{F}_p(x) \equiv \int_0^\infty ds\, s^p/(1+e^{s-x})$ and accurate Padé fits to these integrals and their inverses can be found in [50,51]; an accurate approximation [52] to these fits is given by [53]

$$\lambda_{\rm TF}^{-2} \approx \frac{4\pi e^2 n_e}{\sqrt{T^2 + \left(\frac{2}{3}E_F\right)^2}}, \tag{25}$$

where the Fermi energy of the electrons is given by $E_F = \hbar^2(3\pi^2 n_e)^{2/3}/2m_e$. If it is also necessary to include electronic exchange and correlation effects, a procedure for adding first-order corrections into the screening length can be found in [54]. While (20) is accurate for weakly coupled systems, the DH model overscreens for strong coupling, potentially yielding the unphysical result that the screening length becomes drastically smaller than the interionic spacing.

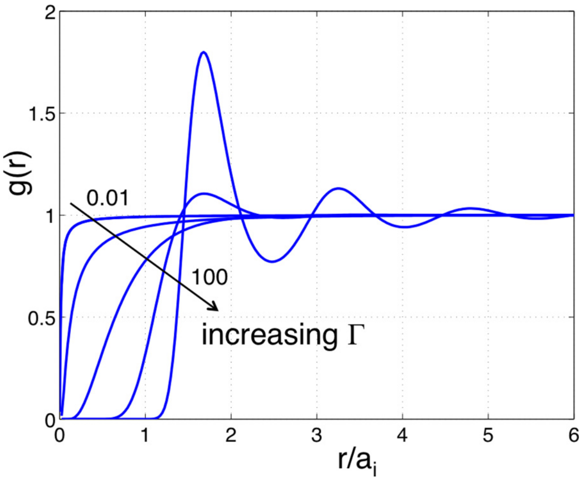

FIG. 5. Radial distribution functions $g(r)$ (in the hypernetted-chain approximation) for a one-component plasma ($\kappa = 0$) with $\Gamma = \{0.01, 0.1, 1, 10, 100\}$. Note that the hole in the ion density around the origin (where there is implicitly an ion) changes very little for $\Gamma > 10$ and that the peak does not shift, revealing that the screening-scale length is approximately a_i over most of the range of strong coupling.

The collapse of the screening length in strongly coupled systems can be avoided by preventing it from dropping below the ion-sphere radius, a behavior consistent with well-known properties of the radial distribution function $g(r)$. This behavior is shown in Fig. 5, where the ionic structure is shown to be dominated by the length scale a_i rather than by the screening length as the coupling is increased. The procedure of transitioning the screening length to the ion-sphere radius at strong coupling is obviously not unique and special care must be taken to choose such a procedure appropriately. In GMS's model [40], a floor on the screening length was enforced by choosing

$$\lambda_{\mathrm{GMS}} = \sqrt{\lambda_e^2 + a_i^2}, \tag{26}$$

although GMS's screening length does not include the DH limit for all species, as in (20), and the prescription is ambiguous in that regard. Alternatively, a simple method suggested by PPFM [5] modifies the screening length to be

$$\lambda_{\mathrm{PPFM}} = \max\{\lambda_{\mathrm{tot}}, a_i\}; \tag{27}$$

however, this form can yield inconsistent results in the limit of weak coupling, especially when electronic screening is strong. This is readily seen by simply taking $\lambda_{\mathrm{ion}} \to \infty$ (that is, vanishing ion screening) and noting that neither (26) nor (27) recovers the correct limit of $\lambda \to \lambda_e$. In this work we present an effective screening length that treats each ionic species separately and recovers the appropriate weakly coupled limits. For one ionic component, this effective length takes the form

$$\lambda_{\mathrm{eff}} = \left(\frac{1}{\lambda_e^2} + \frac{1}{\lambda_i^2 + a_i^2}\right)^{-1/2} \tag{28}$$

$$= \left[\frac{1}{\lambda_e^2} + \frac{1}{\lambda_i^2}\left(\frac{1}{1 + 3\Gamma}\right)\right]^{-1/2}, \tag{29}$$

where the screening length associated with a single ionic species is given in (21) and we have used the definition of the Coulomb coupling parameter $\Gamma = (Z_i e)^2/a_i T$.

These empirical approaches have have been successful in many cases and their phenomenological behavior can be justified by considering the following model. Take a system in which a point source is being screened by both electrons and ions, yet a hole of radius a_i prevents the ions from approaching the source charge. The corresponding Poisson equation, in terms of the electrostatic potential, is given by

$$-\frac{1}{4\pi}\nabla^2\Phi = Z\delta(r) - \frac{\Phi}{4\pi\lambda_e^2} - \frac{\Phi}{4\pi\lambda_{\mathrm{ion}}^2}\mathcal{H}(r - a_i), \tag{30}$$

where $\delta(r)$ is a delta function and $\mathcal{H}(r)$ is the Heaviside step function. Applying the appropriate boundary conditions, the general solution is given by

$$\Phi(r) = \frac{Z}{r} \times \begin{cases} Ae^{r/\lambda_e} + (1 - A)e^{-r/\lambda_e}, & r < a_i \\ Be^{-r/\lambda_{\mathrm{tot}}}, & a_i < r. \end{cases} \tag{31}$$

The coefficients A and B can be solved for by enforcing $\mathcal{C}^1$ continuity in the solution at $r = a_i$. Finally, this ion-hole potential can be expanded about $r = 0$ as

$$\Phi \sim \frac{Z}{r}\left(1 - \frac{r}{\lambda_{\mathrm{IH}}} + \cdots\right) \tag{32}$$

to obtain an effective screening length. Solving for A and B and introducing the standard definition $\kappa \equiv a_i/\lambda_e$, the above expansion yields the expression

$$\lambda_{\mathrm{IH}} = \left[\frac{\lambda_e \sinh(\kappa) + \lambda_{\mathrm{tot}}\cosh(\kappa)}{\lambda_e \cosh(\kappa) + \lambda_{\mathrm{tot}}\sinh(\kappa)}\right]\lambda_e. \tag{33}$$

In the DH limit, where both λ_e and λ_{ion} are large, we recover the relation (20). Furthermore, as $\lambda_e \to \infty$, we obtain $\lambda_{\mathrm{IH}} \sim a_i + \lambda_{\mathrm{ion}}$. While this model provides some insight into the effects of strong coupling on an effective screening length, we have found few quantitative differences in the results obtained using either (28) or (33) and we thus use the simpler λ_{eff} defined in (28) for the remainder of this work.

B. Multicomponent plasmas

While the above quantities are well defined for a single ion species, ambiguities arise in the more general multicomponent case. In particular, we must introduce a definition for the ion-sphere radius of each species that is consistent with the model. Given a system of N species, an approximate representation for the ion-sphere radius of the ith species is

$$a_i = \left(\frac{3Z_i e}{4\pi\rho_{\mathrm{tot}}}\right)^{1/3}, \quad \rho_{\mathrm{tot}} = \sum_{j=1}^{N} Z_j e n_j. \tag{34}$$

This relation is obtained by giving each ion sphere a volume proportionate to its charge such that $V_i/Z_i = V_j/Z_j$, where $V_i = 4\pi a_i^3/3$, and by enforcing the overall volumetric constraint $\sum_i n_i V_i = 1$ as well. Note that (34) reduces to the more common definition for the single-component case [55]. The appropriate effective screening length associated with a multicomponent system of N ionic species is now simply

$$\lambda_{\rm eff} = \left[\frac{1}{\lambda_e^2} + \sum_{i=1}^{N} \frac{1}{\lambda_i^2}\left(\frac{1}{1+3\Gamma_i^{\rm IS}}\right)\right]^{-1/2}. \tag{35}$$

Here the screening lengths are again given by (21) and the coupling parameter of each ionic component $\Gamma_i^{\rm IS}$ is now written in terms of the respective ion-sphere radius, which is now defined by the relation (34) as

$$\Gamma_i^{\rm IS} = \frac{(Z_i e)^2}{a_i T}. \tag{36}$$

While this is not the typical definition for the coupling parameter in mixtures, this is the relevant quantity for the desired physics in the screening length and the usual form is returned in the single-component case. The above relation is connected to the more common definition of the coupling parameter in Sec. V B. Of course, a similar modification can be made to the electronic contribution, but for hot dense matter, electrons are precluded from being too strongly coupled due to their smaller charge and partial degeneracy.

IV. SCREENED COULOMB RESULTS

We now repeat the analysis of Sec. II using the SC potential. This section follows closely the work of Muchmore [39] and Paquette *et al.* [5], who extended the works of Liboff, Kihara, and Aono to include the numerical determination of cross sections and collision integrals. To first illustrate the dramatic effect of incorporating screening into the interaction, a series of trajectories is shown in Fig. 2. Here the screened Coulomb trajectories are seen as dashed curves and are compared to the simpler Coulomb interactions with either a truncated impact parameter (top panel) or a truncated range (bottom panel). The scattering angle of a binary collision will now be given by

$$u_{ij}(r) = \frac{Z_i Z_j e^2}{r} e^{-r/\lambda}, \tag{37}$$

$$\theta_{ij}(b,v) = \pi - 2b \int_{r_0}^{\infty} \frac{dr}{r^2\sqrt{1-(\frac{b}{r})^2 - \frac{2}{\mu v^2}u_{ij}(r)}}, \tag{38}$$

where λ is again the screening length and the distance of closest approach r_0 is now the largest root of the equation

$$1 - \left(\frac{b}{r_0}\right)^2 - \frac{2Z_i Z_j e^2}{\mu v^2 r_0} e^{-r_0/\lambda} = 0. \tag{39}$$

To reduce the size of the parameter space, it is convenient to introduce the transformation and dimensionless parameters

$$r \to \lambda r, \quad \rho = \frac{b}{\lambda}, \quad w^2 = \frac{\lambda \mu_{ij} v^2}{2 Z_i Z_j e^2}. \tag{40}$$

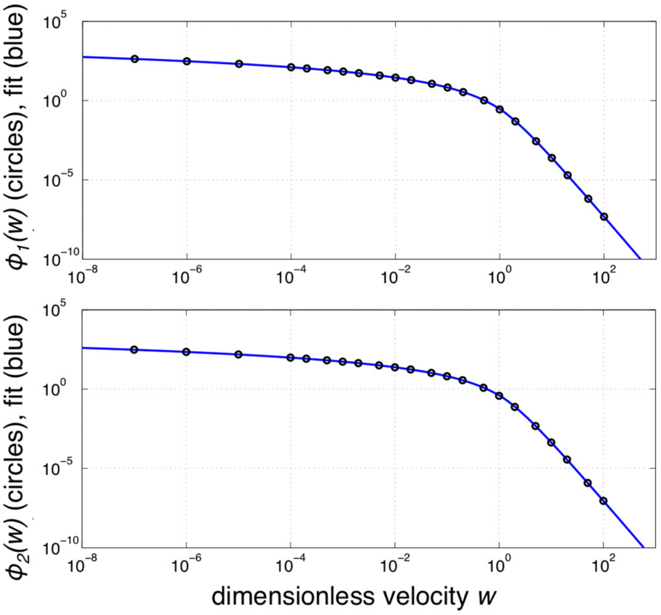

FIG. 6. Reduced cross sections $\phi_n = \sigma_{ij}^{(n)}/2\pi\lambda^2$ versus dimensionless velocity $w = (\mu\lambda/2Z_iZ_je^2)^{1/2}v$ shown for $n = 1$ (top) and $n = 2$ (bottom). The numerical results (black circles) are compared to fits generated with a least-squares method (blue lines); these fits are presented in Eqs. (C15)–(C18).

Generally, there is no closed-form solution to (38). In the weak-scattering approximation, Liboff [28] obtained an approximate scattering angle for the screened Coulomb potential of the form $\theta \sim w^{-2}K_1(\rho)$, where $K_1(\rho)$ is the first-order modified Bessel function of the second kind; however, a full numerical treatment is required to span the parameter space. Consequently, the momentum-transfer cross sections (5) must be calculated numerically as well. The cross sections can be expressed in terms of the dimensionless parameters as

$$\sigma_{ij}^{(n)}(w,\lambda) = 2\pi\lambda^2\phi_n(w). \tag{41}$$

Properties and numerical solutions of $\phi_n(w)$ are presented in Appendix C. Furthermore, Eqs. (C15)–(C18) represent accurate fits to this function, as shown in Fig. 6. We can now compare this result to the cross sections calculated in Sec. II. The dimensionless cross section $\phi_1(w)$ is shown with the Coulomb cross sections with and without velocity-dependent logarithms in Fig. 7. It can be seen that using the velocity-dependent logarithm in (9) recovers the limiting behavior at high velocities but exhibits significant deviation at low velocities. Furthermore, the cross section in (14), which uses a thermal velocity, only recovers mild qualitative agreement for the range of plasma parameters chosen.

Using the same units, we can also express the collision integrals as

$$\Omega_{ij}^{(n,m)} = \sqrt{\frac{2\pi}{\mu_{ij}}}\frac{(Z_iZ_je^2)^2}{T^{3/2}}\mathcal{K}_{nm}(g), \tag{42}$$

$$\mathcal{K}_{nm}(g) \equiv g^m \int_0^{\infty} dw\, e^{-gw^2} w^{2m+3}\phi_n(w), \tag{43}$$

where

$$g = \frac{Z_iZ_je^2}{\lambda T}. \tag{44}$$

The collision integrals are thus entirely characterized by the function $\mathcal{K}_{nm}(g)$. We have provided fits for $\mathcal{K}_{nm}(g)$ in Eqs. (C22)–(C24) in Appendix C as well, where the numerical calculation of $\mathcal{K}_{11}(g)$, along with the corresponding fit, is

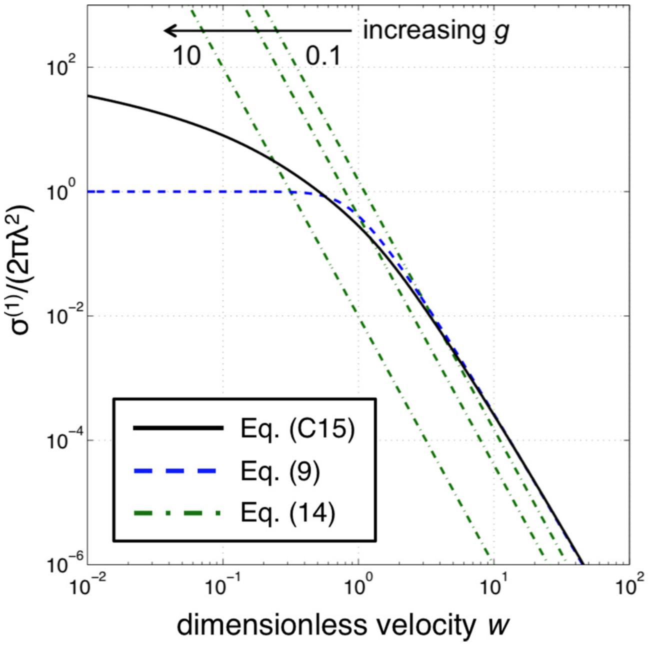

FIG. 7. Comparison of dimensionless cross sections. The screened Coulomb (black solid curve) cross section from Eq. (C15) and the Coulomb cross section using a truncated impact parameter (blue dashed curve), as in Eq. (9), have the same limiting behavior at high velocities but deviate significantly from each other at low velocities. The Coulomb cross section using a thermal velocity in the logarithm, as in Eq. (14), is shown for several plasma parameters (green dash-dotted curve), for a range of values of $g = \{0.1, 1, 10\}$.

shown in Fig. 8. To compare these calculations to the simpler CL results, it is convenient to plot the ratios of the collision integrals, which allows these quantities to be represented in terms of the plasma parameter g alone. The ratios of the full collision integral, using the SC potential within the EB approach, to the collision integrals calculated from the cross sections (9), (14), and (16) are shown in Fig. 9. Note that significant deviation from unity is seen for each approximation at even smaller values of the plasma parameter g.

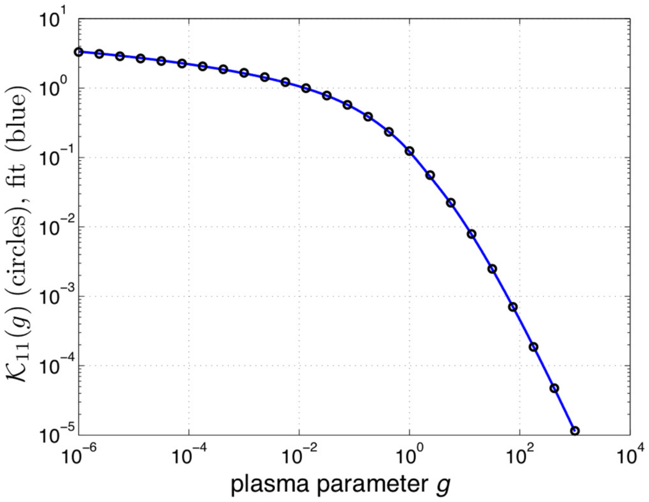

FIG. 8. Reduced collision integral (43) as a function of the plasma parameter $g = Z_i Z_j e^2/\lambda T$ for the case $(n,m) = (1,1)$. The numerical results (black circles) are compared to fits generated with a least-squares method (blue lines); these fits are shown in Eqs. (C22)–(C24). The cases of (1,2), (1,3), and (2,2) yield visually similar results and have been omitted for brevity.

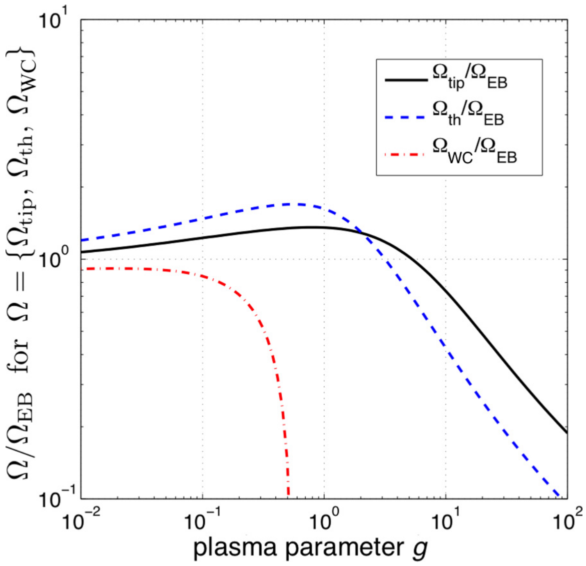

FIG. 9. Comparison of collision integrals as ratios of these integrals to the EB collision integral calculated from (42). Here $\Omega_{\rm tip}$ (black solid curve) is calculated using the cross section with a truncated impact parameter in (9), $\Omega_{\rm th}$ (blue dashed curve) is calculated using the cross section with a thermal velocity in (14), and $\Omega_{\rm WC}$ (red dotted curve) is calculated using the cross section in the weakly coupled limit from (16). Each approximation results in significant deviations from unity for even smaller values of the plasma parameter g.

V. TRANSPORT COEFFICIENTS

High-energy-density environments are most typically modeled using the macroscopic equations of hydrodynamics [56–58]. When mild kinetic effects are important, HED matter can be modeled by the Fourier-Navier-Stokes equations (FNSEs)

$$\frac{\partial \rho_i}{\partial t} + \nabla \cdot (\rho_i \mathbf{v}) = \nabla \cdot D_{ij}[x_j \nabla \rho_i - x_i \nabla \rho_j], \tag{45}$$

$$\rho\left(\frac{\partial \mathbf{v}}{\partial t} + \mathbf{v} \cdot \nabla \otimes \mathbf{v}\right) = -\nabla P + \eta \nabla^2 \mathbf{v}, \tag{46}$$

$$\frac{\partial T_i}{\partial t} = \frac{1}{C_V} \nabla \cdot (K_i \nabla T_i) + \sum_j \frac{1}{\tau_{ij}} (T_j - T_i) + S_i, \tag{47}$$

which are the usual three conservation laws for a mixture. Note that ρ represents the *mass* density in this section, whereas it represents the *charge* density elsewhere in this work. These equations describe the time evolution of a mixture subject to pressure forces but also include diffusive mixing, viscosity, thermal conduction, temperature relaxation, and possibly an external energy source or sink. As is common, there is one momentum equation, representing the total momentum of the mixture. This form is generic and the detailed material properties enter through choices of the equation of state and of the transport coefficients. Obviously, when the transport coefficients are small, this set of equations becomes the simpler Euler hydrodynamics equations [59]; conversely, for hot dense matter, accurate models require knowledge of the transport coefficients because they are moderate to large. In fact, at very high temperature [60], or when there are steep gradients [61], the FNSE description itself may become inadequate as nonlocal transport becomes important; such circumstances are beyond the scope of the present work, but see the discussion around (83) below.

In previous sections, we have provided an effective potential approach to computing the transport coefficients for processes involving ion-ion collisions and the results have been reduced to simple fits in (C22)–(C24). In this section we will discuss each transport coefficient in turn. We begin in the next subsection with the self-diffusion coefficient, which, while it does not appear in (45)–(47), provides the simplest test of the models, and we have generated MD data to validate our result for this coefficient. In the following subsections we discuss interdiffusivity, viscosity, and thermal conductivity and we validate our predictions with the MD results of several investigators.

A. Self-diffusivity

The simplest transport process is self-diffusivity, which describes the movements of tagged individual particles from regions of high concentration to regions of low concentration. To linear order, this can be represented in terms of gradients of the mass density ρ, as Fick's first law

$$\mathbf{J} = -D\nabla\rho, \tag{48}$$

where $\mathbf{J}$ is the the mass flux and D is the self-diffusion coefficient. To validate the EB model for D, we compare with the more fundamental Green-Kubo relation

$$D = \frac{1}{3}\int_0^\infty dt\,\langle \mathbf{v}(t)\cdot\mathbf{v}(0)\rangle, \tag{49}$$

where $\mathbf{v}$ is the velocity of a particle and the angular brackets correspond to both an average over particles and equivalent initial times of the stationary ensemble. It is useful to define the velocity autocorrelation function (VACF)

$$Z(t) = \frac{\langle \mathbf{v}(t)\cdot\mathbf{v}(0)\rangle}{\langle \mathbf{v}(0)\cdot\mathbf{v}(0)\rangle}, \tag{50}$$

which is a normalized measure of the collision dynamics of individual particles over time; note that

$$D = \frac{T}{m}\int_0^\infty dt\, Z(t). \tag{51}$$

We will examine detailed properties of $Z(t)$ in Sec. VI.

The particle trajectories needed to evaluate $Z(t)$ are readily obtained from MD; here we have used a standard methodology with interionic potentials of the form

$$u(r) = \frac{Z^2e^2}{r}e^{-r/\lambda_e}. \tag{52}$$

Note that (52) contains *only* the electronic screening length, as the many-body effects of the ions are included naturally in the MD simulation. While many authors have computed the self-diffusion coefficient for Yukawa systems, we validated our MD using the results of Ohta and Hamaguchi [62]; we also extended the work of these authors to weaker coupling, where the transport coefficients are large, and our results are therefore relevant to HED applications. In particular, we focused on plasma conditions for which there are important differences in CL prescriptions.

As usual, we characterize the plasma using the standard dimensionless quantities

$$\Gamma = \frac{Z^2e^2}{a_iT}, \quad \kappa = \frac{a_i}{\lambda_e}, \tag{53}$$

where Γ is the Coulomb coupling parameter. The plasma parameter, which is the principle input to the collision integrals, can be expressed in terms of these quantities as

$$g = \frac{Z^2e^2}{\lambda_{\text{eff}}T} = \Gamma\left(\kappa^2 + \frac{3\Gamma}{1+3\Gamma}\right)^{1/2}. \tag{54}$$

Molecular-dynamics simulations were carried out for the parameter values listed in Table I to yield dimensionless self-diffusivities $D^* = D/\omega_p a_i^2$, where a_i is the ion-sphere radius and $\omega_p = (4\pi n Z^2e^2/m_i)^{1/2}$ is the plasma frequency. The MD results were then compared to the first-order CE prediction of the self-diffusivity

$$D = \frac{3T}{8nm_i\Omega_{ii}^{(11)}} = \frac{3T^{5/2}}{16\sqrt{\pi m_i}nZ_i^4e^4\mathcal{K}_{11}(g)}, \tag{55}$$

which in its reduced form is given by

$$D^* = \frac{\sqrt{3\pi}}{12\Gamma^{5/2}\mathcal{K}_{11}(g)}. \tag{56}$$

TABLE I. Results from molecular-dynamics calculations of the self-diffusion coefficient $D^* = D/\omega_p a^2$ are given for ranges of κ and Γ. These results are shown and compared with theoretical models in Fig. 10.

κ	Γ	D^*	κ	Γ	D^*
0.5	0.1	143	1.5	0.1	209
	0.3	16.4		0.3	24.5
	0.5	6.4		0.5	10
	0.7	3.76		0.7	5.92
	1.0	2.14		1.0	3.15
	2.0	0.82		2.0	1.19
	5.0	0.28		5.0	0.356
	10.0	0.13		10.0	0.155
	20.0	0.069		20.0	0.0787
	30.0	0.043		30.0	0.0505
1.0	0.1	173	2.0	0.1	241
	0.3	20.9		0.3	28.4
	0.5	8.41		0.5	12.3
	0.7	4.72		0.7	7.32
	1.0	2.54		1.0	3.72
	2.0	1.02		2.0	1.52
	5.0	0.31		5.0	0.504
	10.0	0.15		10.0	0.229
	20.0	0.073		20.0	0.0998
	30.0	0.0456		30.0	0.0681

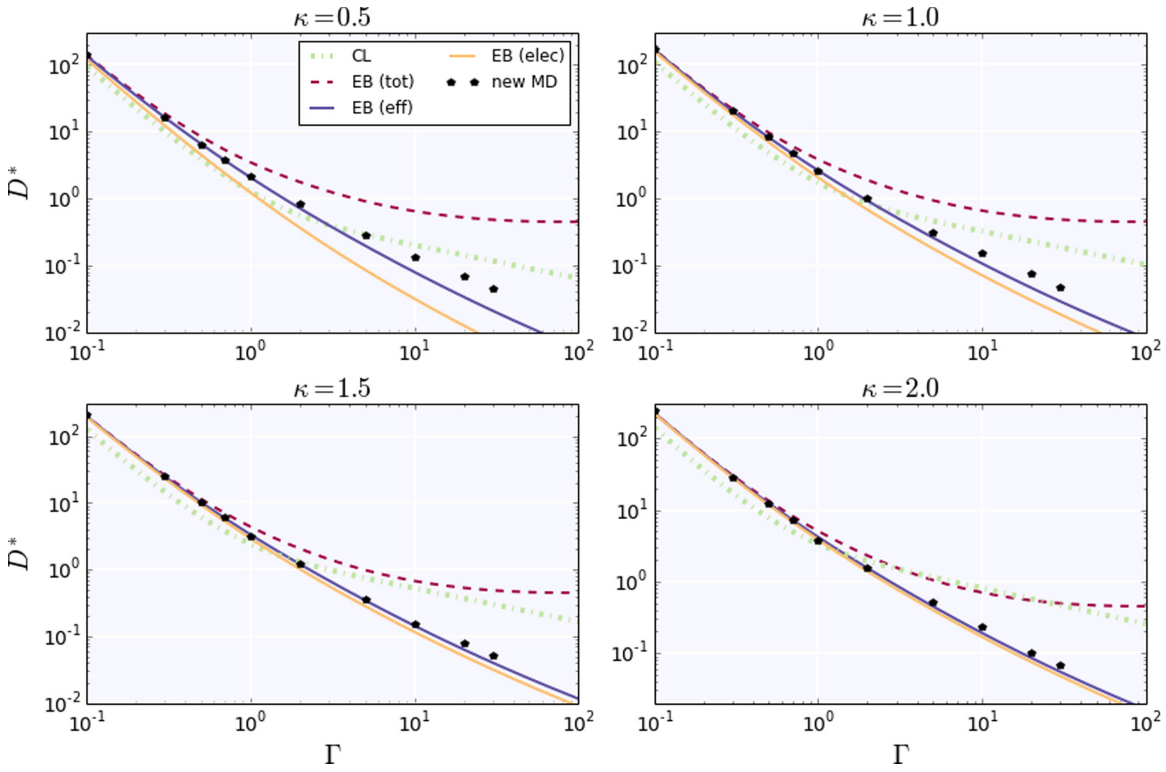

FIG. 10. Self-diffusion coefficient $D^* = D/\omega_p a^2$ versus Γ for $\kappa = \{0.5, 1.0, 1.5, 2.0\}$. Shown are three variants of the EB approach based on an electron-only screening length (solid yellow curve), the total DH screening (dashed red curve), and the effective screening length of (28) (solid blue curve). Black points are our MD results. Also shown are the results obtained using the CL of (15) (dash-dotted green curve).

We can define an effective diffusion CL as $\ln \Lambda_D \equiv 4\mathcal{K}_{11}$ to recover the more familiar expression for the self-diffusion coefficient.

Our results are shown in Fig. 10, where we compare MD with EB for three choices of the effective potential—electron-only screening, total DH screening, and the effective screening of (28)—and the CL of (15) using the screening length in (28). Compared with MD, the electron-only screening model, shown as a solid yellow line, does a fair job, especially when the electron screening is strong (large κ). This trend is expected because the electrons dominate screening when κ is large unless the ions are very strongly coupled. Including the ions in the screening length according to (20) yields the dashed red curve, which represents a very slight improvement for small Γ but is considerably worse for large Γ. This trend can be seen in Fig. 11, where an expanded view of the weak-coupling region is shown, now on a log-linear scale. However, with the modification of (28), excellent agreement with MD is found over most of the ranges of Γ and κ. These results can be understood as follows. When κ is small, ionic screening contributes substantially to the overall effective potential; however, as the coupling becomes modest to large, the DH model for the ions overscreens and the additional contribution of a_i in (28) becomes very important. We would like to point out that the trend seen in this figure occurs in part because the ionic Γ is allowed to vary while the electron screening κ is being held fixed; in a real plasma, a much more complex interplay between these parameters would occur.

B. Atomic-scale diffusive mixing

Atomic-scale mixing between species is described in the FNSE model through terms in (45) that contain the interdiffusion terms involving the coefficients D_{ij}. Preventing such material mixing at interfaces in ICF experiments is essential to ensure a clean fuel region. Because interdiffusion is sufficiently different from self-diffusion, we present here some of the important definitions needed when considering interdiffusion before discussing numerical results.

For simplicity, consider a binary mixture with species number densities n_1 and n_2, total number density $n = n_1 + n_2$, masses m_1 and m_2, total mass density $\rho = \rho_1 + \rho_2 = m_1 n_1 + m_2 n_2$, and charges $Z_1 e$ and $Z_2 e$. Using these quantities, we can form the fractional densities $c_i(\mathbf{r},t) = n_i(\mathbf{r},t)/n(\mathbf{r},t)$ and $x_i(\mathbf{r},t) = \rho_i(\mathbf{r},t)/\rho(\mathbf{r},t)$. The mixing rate for species i can be written using the continuity equation

$$\frac{\partial \rho_i}{\partial t} + \nabla \cdot (\rho_i \mathbf{u}) = -\nabla \cdot \mathbf{J}_i, \qquad (57)$$

which is written in terms of the center-of-mass velocity field

$$\mathbf{u}(\mathbf{r},t) = \sum_j x_j(\mathbf{r},t)\mathbf{u}_j(\mathbf{r},t), \qquad (58)$$

which is in turn written in terms of the local velocity fields $\mathbf{u}_j(\mathbf{r},t)$. The mass flux in excess of the inertial convection for each species is then

$$\mathbf{J}_i(\mathbf{r},t) = \rho_i(\mathbf{r},t)[\mathbf{u}_i(\mathbf{r},t) - \mathbf{u}(\mathbf{r},t)]. \qquad (59)$$

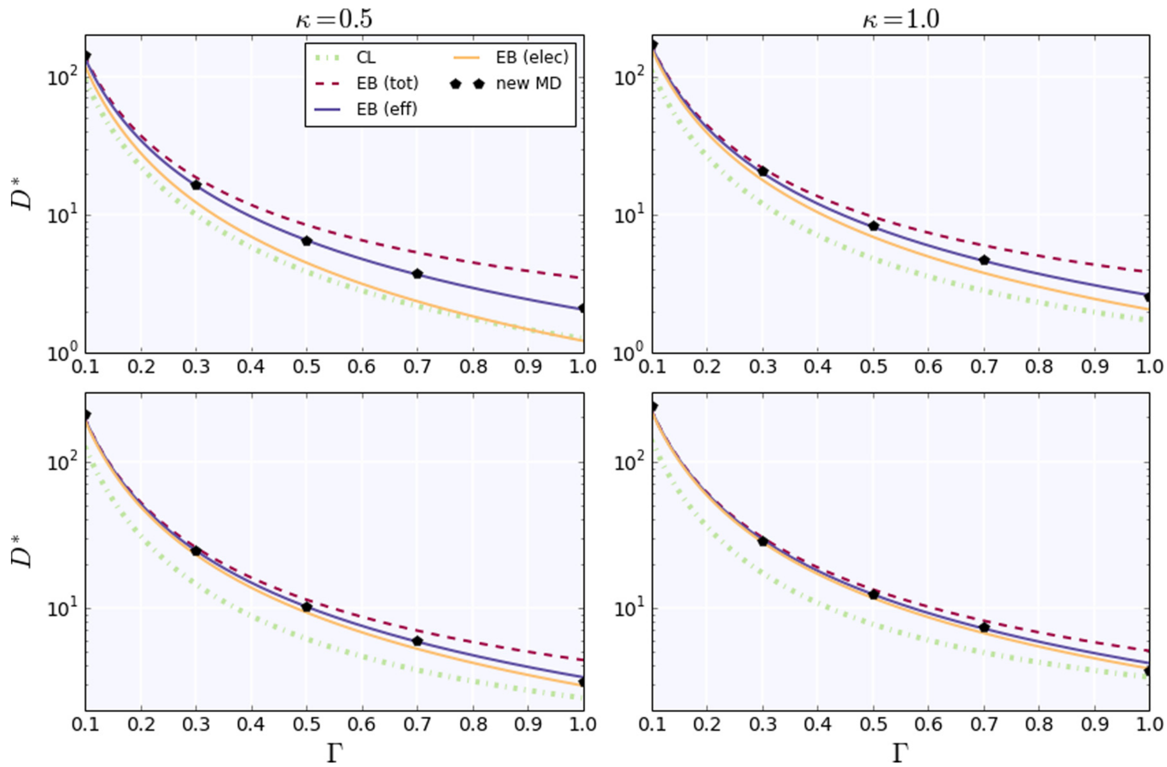

FIG. 11. Same quantities as in Fig. 10, but shown here using an abbreviated linear scale for Γ to emphasize the weak-coupling limit.

Using the conservation of the total density $\rho(\mathbf{r},t)$, we can also express (57) as

$$\rho\left[\frac{\partial x_i}{\partial t} + \mathbf{u}\cdot\nabla x_i\right] = -\nabla\cdot\mathbf{J}_i. \tag{60}$$

These relations, which are microscopically exact, are simply expressions of species continuity written in terms of variables relevant to mixing.

If we assume time scales such that momenta have reached a steady state and the only gradients present are the concentration gradients, we can approximate the mass fluxes using the relation

$$\begin{aligned}\mathbf{J}_i &\equiv -\rho(\mathbf{r},t)D_{ij}\nabla x_i(\mathbf{r},t) &(61)\\ &= -D_{ij}[x_j(\mathbf{r},t)\nabla\rho_i(\mathbf{r},t) - x_i(\mathbf{r},t)\nabla\rho_j(\mathbf{r},t)], &(62)\end{aligned}$$

which serves to define the interdiffusion coefficient D_{ij} [63]. Given the total flux balance $\mathbf{J}_1 + \mathbf{J}_2 = \mathbf{0}$, it must then be true that $D_{ij} = D_{ji}$. (However, we will retain the subscripts to distinguish this coefficient from the self-diffusion coefficient.) In general, D_{ij} is a complicated function of the local properties of a dense plasma mixture. In the limit in which the nonlinear advection term in (60) is negligible, (45) decouples from (46) to yield

$$\frac{\partial\rho_i}{\partial t} = \nabla\cdot D_{ij}[x_j\nabla\rho_i - x_i\nabla\rho_j]. \tag{63}$$

Note that unlike with self-diffusion, density fluctuations in ρ_i can arise from inhomogeneities in the jth species, even if the ith species is itself uniform. If we additionally approximate the mean total density $\rho(\mathbf{r},t)$ to be a constant, we obtain the simpler form of

$$\frac{\partial x_i}{\partial t} = \nabla\cdot D_{ij}\nabla x_i, \tag{64}$$

which describes the change in the relative concentration of species i due to its gradient. These nonlinear diffusion equations are analogous to those obtained by Molvig *et al.* [60]. However, note that (63) is a set of *coupled* diffusion equations for the two species and, despite its simple appearance, (64) is coupled to the evolution equation for x_j as well because $D_{ij} = D_{ij}(x_i,x_j)$. For example, note that collision rates of species i will depend on the screening properties of species j, through the effective potential, and therefore on the temperature, density, and charge of species j as well. In modeling real experiments, of course, the steady-state assumption (62) obviates the use of such diffusion equations for short times, the flux in (62) may involve other gradients, the nonlinear advection terms may not be negligible, and the total mean density may not be nearly uniform; in such cases, (46) must be solved simultaneously with (45). When (62) is used to model the relative fluxes, the atomic mixing problem reduces to the solution of nonlinear diffusion equations that require D_{ij} values, which can be written as

$$\begin{aligned}D_{ij} &= \frac{3T}{16n\mu_{ij}\Omega_{ij}^{(11)}} &(65)\\ &= \frac{3T^{5/2}}{16\sqrt{2\pi\mu_{ij}}nZ_i^2Z_j^2e^4\mathcal{K}_{11}(g)}, &(66)\end{aligned}$$

where the collision integral $\Omega_{ij}^{(11)}$ is given by (6).

To validate our numerical results, we have chosen to compare with the MD results of Hansen, Joly, and McDonald

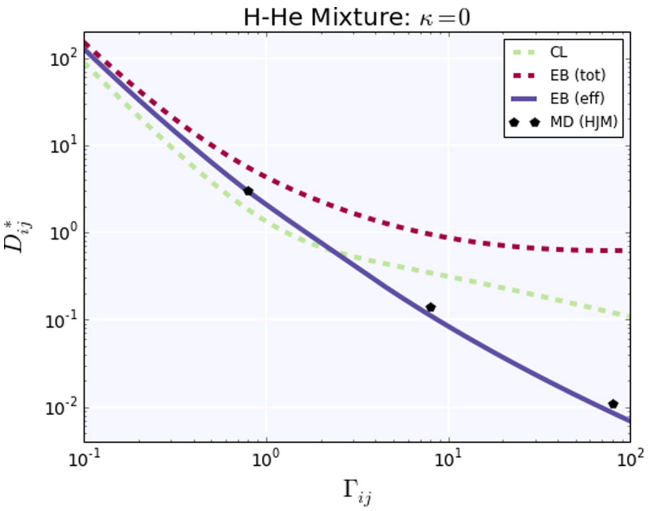

FIG. 12. Comparison of our EB solution of the interdiffusion coefficient to MD data from [64]. Two models for the effective screening length are used: total (red dashed curve) and effective (blue solid curve).

(HJM) for dense plasma mixtures relevant to stellar interiors [64]. The case of HJM was chosen in part because these investigators employed the binary-ionic mixture, in which the ions interact through a bare Coulomb force. That is, in this case, there is no electron screening contribution in (28), or equivalently $\kappa = 0$; the effective screening length is thus determined by the self-screening of the ions alone. A 50/50 mixture of H^+ and He^{2+} was used for the three values of $\Gamma_{ij} = \{0.8, 8, 80\}$, where $\Gamma_{ij} = Z_i Z_j e^2/a_{\text{tot}}T$, with $a_{\text{tot}} = (3/4\pi n_{\text{tot}})^{1/3}$ and $n_{\text{tot}} = n_{\text{H}} + n_{\text{He}}$. In these units, the plasma parameter can be written as

$$g = \frac{Z_i Z_j e^2}{\lambda_{\text{eff}} T} \tag{67}$$

$$= \Gamma_{ij}\left(\kappa^2 + \sum_{k=1}^{N} \frac{3x_k^{-1}\Gamma_{kk}}{1 + 3(x_k/z_k)^{1/3}\Gamma_{kk}}\right)^{1/2}, \tag{68}$$

where now $\kappa = a_{\text{tot}}/\lambda_e$, $x_i = n_i/n_{\text{tot}}$ is the number-density concentration, and $z_i = \rho_i/\rho_{\text{tot}}$ is the charge-density concentration. In Fig. 12 we show comparisons with the MD results of HJM for this case and with two EB results using the total DH screening length and the effective screening length of (28). In this case of a mixture, the coefficient is normalized as $D^* = D/\omega_{\text{HP}} a_{\text{tot}}^2$, where the hydrodynamic plasma frequency ω_{HP} is defined in terms of the mean charge and mean mass of the mixture. Once again, we see excellent agreement between MD results and the effective model and the usual DH screening model fails for moderate coupling.

C. Viscosity coefficient

We now turn to macroscale mixing. When a high-density fluid is accelerated by a low-density fluid, an interfacial fingering instability known as the Rayleigh-Taylor instability (RTI) occurs [65–68]. In an imperfect ICF capsule, small-scale perturbations between the ablator and fuel layers can grow to large amplitudes and potentially result in a turbulent state. In a simple fluid model, in which the amplitude of the interfacial perturbation is given by h, the growth of instability can be approximately modeled as

$$\frac{dh}{dt} = \alpha h, \tag{69}$$

where the growth rate α is a function of the physical properties of the plasma and the forces. The simplest model for the growth rate $\alpha_0(k)$ is given by

$$\alpha_0(k) = \sqrt{Agk}, \tag{70}$$

where $A = (\rho_1 - \rho_2)/(\rho_1 + \rho_2)$ is the Atwood number in terms of the two fluid densities ρ_1 and ρ_2, g is the acceleration, and k is the wave number of the interfacial disturbance. This formulation of RTI does not include the effects mentioned in the previous section; however, Duff *et al.* [69] developed a model for instability growth that includes both diffusive and viscous corrections. In the absence of diffusion, they employ the approximate result

$$\alpha_\nu = (Agk + \nu^2 k^4)^{1/2} - \nu k^2, \tag{71}$$

where $\nu = (\eta_1 + \eta_2)/(\rho_1 + \rho_2)$ is the mean kinematic viscosity in terms of the densities and viscosities of each material. As is well known, viscosity generally suppresses instability growth at shorter length scales and this is increasingly true for larger viscosities. Similarly, when the effects of diffusion are included, the total growth rate becomes

$$\alpha_{\nu D} = [Agk/\psi + \nu^2 k^4]^{1/2} - (\nu + D)k^2, \tag{72}$$

where ψ is a known function of A, k, and D [69]. Thus, accurate values of the material viscosities and diffusivities are needed to understand and model RTI growth rates. Because diffusion can be slow, mixing is often dominated by fluid instabilities, in which case we can characterize the impact of transport on RTI by scaling the growth rate (71) by (70) to obtain

$$\frac{\alpha(k)}{\alpha_0(k)} = \sqrt{1 + \tilde{\nu}^2 \tilde{k}^3} - \tilde{\nu}\tilde{k}^{3/2}, \tag{73}$$

where $\tilde{\nu} = \nu/\nu_e$ is in terms of ν_e, the viscosity computed using the electron screening length, and $\tilde{k} = k/(Ag/\nu_e)^{1/3}$. Framed this way, we can examine the role of viscosity in terms of different choices for the effective potential, using

$$\eta = \frac{5T}{8\Omega_{ii}^{(22)}} = \frac{5\sqrt{m_i}T^{5/2}}{16\sqrt{\pi} Z_i^4 e^4 \mathcal{K}_{22}(g)}. \tag{74}$$

Alternatively, the reduced viscosity is given by

$$\eta^* = \frac{5\sqrt{3\pi}}{36\Gamma^{5/2}\mathcal{K}_{22}(g)}, \tag{75}$$

where $\eta^* = \eta/mn\omega_p a^2$. Note that $\mathcal{K}_{22}(g)$ can be thought of as an effective Coulomb logarithm for viscosity, as

$$\ln \Lambda_\eta \equiv 2\mathcal{K}_{22}(g), \tag{76}$$

for which the numerical results above can be used. Given that the cross section $\sigma^{(2)}(v)$ must be used for this transport process, the CL with an impact parameter cutoff and a thermal velocity

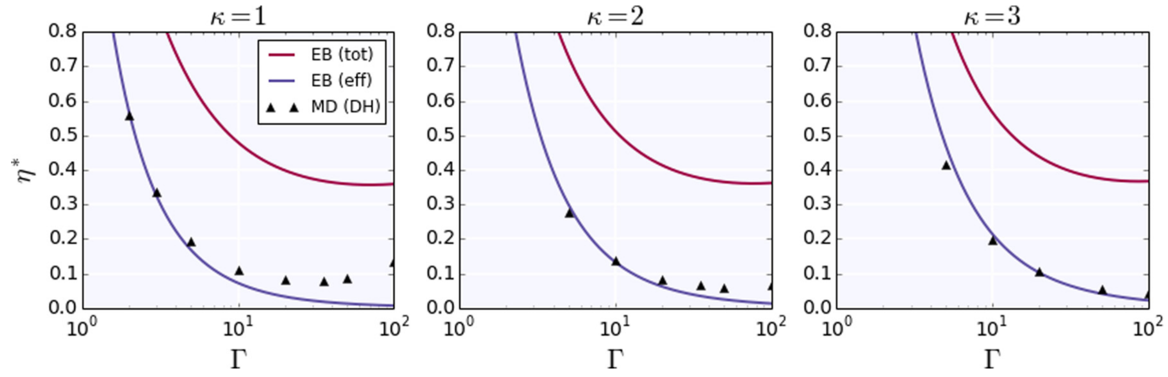

FIG. 13. Dimensionless viscosity $\eta^* = \eta/mn\omega_p a^2$ shown for $\kappa = \{1,2,3\}$ using the MD data of Donko and Hartmann (black triangles) [70] and the EB approach with both the total screening length (red upper curve) and the effective screening length of (28) (blue lower curve). The effective screening length result agrees well with the MD data for $\Gamma < 10$ at $\kappa = 1$ and for even larger values of Γ as κ increases, to nearly $\Gamma \sim 100$ with $\kappa = 3$.

analogous to (15) is given by

$$\ln \Lambda^{(2)}_{\text{hyp}} = \frac{1}{2}\left[\ln\left(1 + \frac{4}{g^2}\right) + \frac{4}{4+g^2}\right]. \tag{77}$$

This illuminates the important point that different CLs must be used for different transport processes. Even within the binary framework of the EB approach, the collision integrals clearly change, as indicated by the indices (n,m). Generally, the effective Coulomb logarithm associated with the index pair (n,m) can be expressed in terms of the function (43) as

$$\ln \Lambda^{(n,m)} = \frac{4\mathcal{K}_{nm}(g)}{n(m-1)!}. \tag{78}$$

Our results are shown in Fig. 13, where we plot the dimensionless viscosity η^* versus Γ for the three values of $\kappa = \{1,2,3\}$. We compare MD results from [70] to the EB predictions using the total and effective screening lengths. Once again, we see much better agreement using (28) relative to the total DH screening length. In the case of viscosity, we see especially poor agreement for very strong coupling and this behavior differs from that observed with the other coefficients presented above. This failure can be traced to the fact that the Boltzmann equation is incapable of describing correlations in systems poorly modeled by the ideal gas equation of state and binary collisions. However, in the regimes most relevant to HED materials, for which the viscosity is large, the agreement between the MD and EB results is very good.

D. Thermal conductivity

The transport coefficients discussed above are associated with particle and momentum transport. Equally important is the transport of heat (or temperature or energy). Short-pulse laser-target interactions are an important class of applications in which large amounts of energy are rapidly absorbed in a small region of a target. These applications include laser ablation of metals [71], ICF [72,73], and x-ray laser deposition [74]. When heating is rapid, there may be little mass motion and the full set of equations (45)–(47) may not be needed. Under such circumstances, only (47) is needed; such a model that includes radiation absorption is given by the electron-ion two-temperature model (TTM) [15,75,76], which includes the coupled energy equations

$$\frac{\partial T_e}{\partial t} = \frac{1}{C_e}\nabla\cdot(K_e\nabla T_e) + \frac{1}{\tau_{ie}}(T_i - T_e) + S_{\text{rad}}, \tag{79}$$

$$\frac{\partial T_i}{\partial t} = \frac{1}{C_i}\nabla\cdot(K_i\nabla T_i) + \frac{1}{\tau_{ie}}(T_e - T_i), \tag{80}$$

which are a variant of coupled nonlinear reaction-diffusion equations for the electron and ion temperatures. In this TTM, it is assumed that the radiation is absorbed into the electrons only and is included through the source term $S_{\text{rad}}(t)$. More advanced versions of the TTM replace the ion temperature equation (80) with a full MD description [71]. More complete models used for ICF include the full set of hydrodynamic equations [73], as in (45)–(47), but also include an additional radiation-diffusion equation. The thermal conductivities K_e and K_i for the electrons and ions, respectively, obviously play a key role in the distribution of energy in these models. (The temperature relaxation term is discussed elsewhere [25,40].)

Here we focus on the ion thermal conductivity, as our approach is most applicable to ionic transport; the general conclusions will apply to electron heat conduction as well, which can be treated with a cross-section calculation for attractive quantum scattering [77]. The EB thermal conductivity is given by

$$K = \frac{75T}{32m_i\Omega^{(22)}_{ii}} = \frac{75T^{5/2}}{64\sqrt{\pi m_i}Z_i^4e^4\mathcal{K}_{22}(g)}, \tag{81}$$

which is in terms of the same collision integral $\Omega^{(22)}_{ii}$ as the viscosity (to this order) and thus the ratio (proportional to the Prandtl number) is independent of details of the collisions. Alternatively, the reduced conductivity is given by

$$K^* = \frac{25\sqrt{3\pi}}{48\Gamma^{5/2}\mathcal{K}_{22}(g)}, \tag{82}$$

where $K^* = K/m\omega_p a_i^2$. Our results are shown in Fig. 14 for various values of Γ and κ. We also show a fit to previous MD data [78] as a solid black line; a dashed black line is used to denote regions in which the fit is an extrapolation of the MD data. Our numerical result has a different scaling with

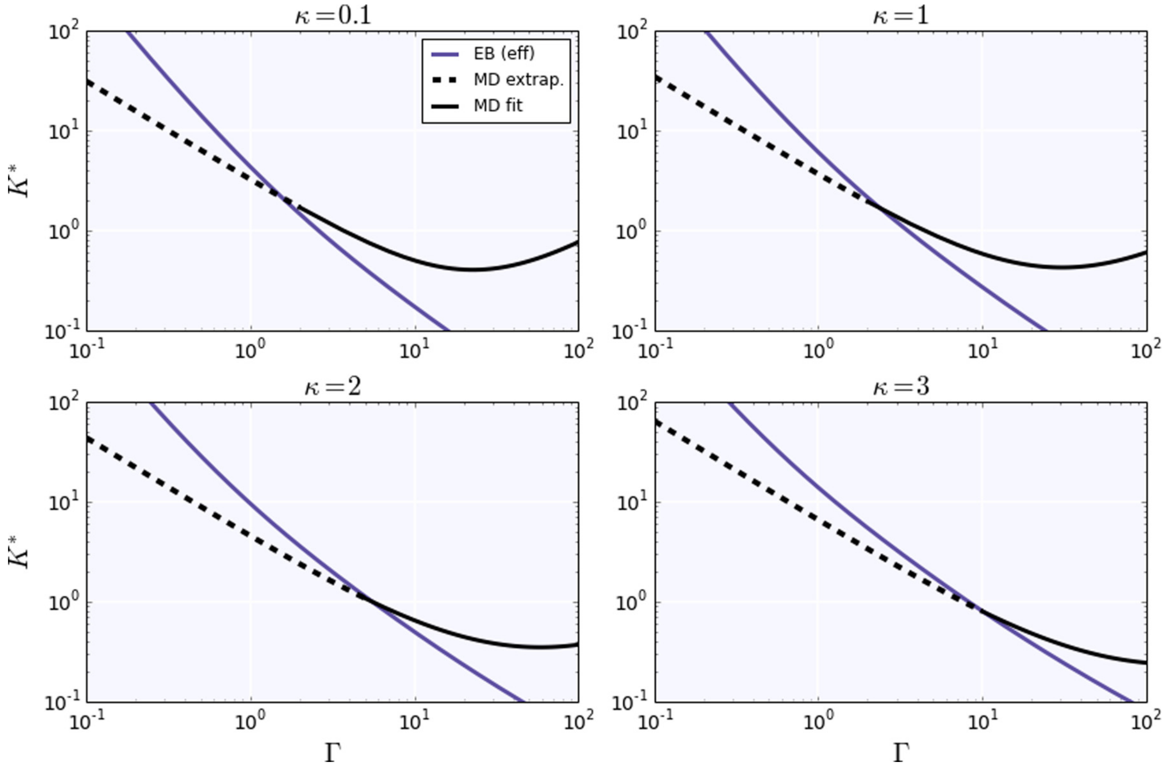

FIG. 14. Dimensionless thermal conductivity K^* versus Γ for four values of $\kappa = \{0.1,1,2,3\}$. The EB result using (28) is shown as a solid blue line. A fit to MD results [78] is shown in black; we use a solid line for the fit over the Γ range where MD results contributed to the fit and a dashed line in the range where the fit is extrapolated, revealing the large error associated with extrapolating MD results to weak coupling. For this transport coefficient, the MD fit provides much less of a validation than for the others.

Γ at weak coupling, revealing a transition of behavior in the moderate-coupling regime; MD fits obtained in the strongly coupled regime should not be extrapolated. As with the viscosity, our results do not capture the thermal-conductivity minimum; however, as we mention above, when values of the transport coefficients are very small, they are relatively less important to the overall hydrodynamics, so this does not represent a serious limitation. Importantly, the MD data does not exist at sufficiently small couplings to validate the model in the same way as the other transport coefficients discussed above. This suggests the need for further MD studies of thermal conductivity, which is notoriously difficult to compute [79].

It is important to note that heat conduction, because it involves a larger velocity moment, can become nonlocal [80] when there is a steep gradient, thereby obviating the form of the TTM given above. Under such circumstances, however, our approach can still be used to give approximate results in nonlocal kernel models, such as models of heat flux of the form [80,81]

$$q(z) = \int dz' G(z,z')\, q_{\rm local}(z'), \tag{83}$$

where $G(z,z')$ describes the nonlocality and $q_{\rm local}$ is a local approximation. The local flux, given by Fourier's law, could employ the thermal conductivity coefficient described in the present work; however, additional work in this area is warranted, especially for the electron-ion scattering case.

VI. EFFICACY OF THE EFFECTIVE BINARY APPROACH

The effective Boltzmann approach based on (B1) and (18) cannot describe the collective dynamics of a many-body system. In the LB branch of Fig. 1, dynamical effective potentials are of the form $v(k)/\epsilon(k,\omega)$, where $\epsilon(k,\omega)$ is the frequency-dependent dielectric response function; such effective potentials incorporate hydrodynamic waves and flows, as well as finite-velocity effects. For example, in the effective potential approach of Grabowski *et al.* to describing stopping power [27], a finite-velocity correction to the effective potential was essential. Because a *static* effective potential used in a Boltzmann (CE) approach cannot easily handle many-body *dynamics*, we wish to estimate the importance of such effects, which we do in the context of the self-diffusion coefficient. (See Appendix B for further details of the Boltzmann approach.)

We begin by noting that the Boltzmann equation effectively describes very short-time scattering events; the derivation of the Boltzmann equation, as with most collision operators, assumes a Bogolyubov separation of time scales between the one- and two-body distribution functions. Moreover, the randomization (stosszahlansatz) incorporated into the boundary conditions of the collision process results in a Markov process. Taken together, this predicts a simple exponential decay of the VACF. Modifying the force law, as in the choice of the effective potential, does not impact these properties of the Boltzmann equation. Thus, the appearance of non-Markovian features reveals a breakdown of the effective Boltzmann approach

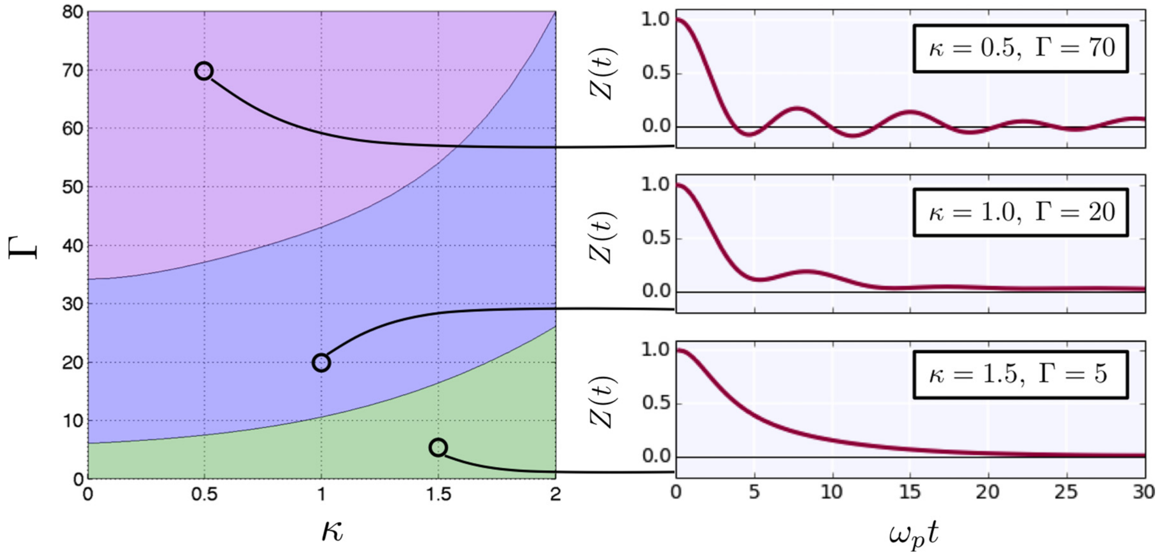

FIG. 15. Variation in functional forms of the VACF. In the left panel, the Yukawa phase diagram for three different behaviors is shown: the bottom (green) region is exponential decay, the middle (blue) region is the modulated decay regime in which oscillations in the VACF begin to arise, and the top (purple) region is the caged regime. In the right panel, we show several characteristic VACFs across the phase diagram corresponding to the (κ,Γ) values of (0.5,70), (1,20), and (1.5,5), respectively.

and this breakdown is readily observed in the MD results. We have computed the VACF over a wide range of the (Γ,κ) parameter space and have examined its decay properties. These results are summarized in Figs. 15 and 16. In Fig. 15 we show the Yukawa phase diagram with three regions shaded. In the lower (green) region, the VACF decays monotonically to zero. For very weak coupling, the decay is visibly exponential, although a ballistic behavior at early time becomes observable as the effective coupling is increased. One expects that the EB approach would model this regime quite well. In the middle (blue) region, the VACF is always positive at early times ($\omega_p t < 30$) but exhibits an onset of oscillations: The decay is no longer monotonic, revealing a feature not well described using a Boltzmann approach. The collective dynamics are occurring on the same time scale as the collision itself. As we have seen in the previous section, we get reasonable agreement in this regime, perhaps because the decay is similar enough to the simpler exponential decay. We have defined the boundary between these two regions as being the point at which the first oscillation in the VACF has a zero derivative and an approximate representation of this boundary in the range $\kappa \in [0,2]$ is given by

$$\Gamma_{\rm osc} \approx 5.97 + 1.93\kappa + 1.16\kappa^2 + 1.44\kappa^3. \tag{84}$$

Because the modulated decay region occurs for modest values ($\Gamma > 5.97$) of the Coulomb coupling, it only impacts transport when the transport coefficients are modest to small. Finally, in the top (purple) region, we have the so-called caging regime, in which the VACF changes sign, indicating a reversal of the direction of the ion. Caging implies quite strong coupling, as each particle is temporarily trapped by the cage formed by its (several) neighbors, a phenomenon clearly incapable of being described appropriately by considering binary cross sections. As seen in the previous section, the effective Boltzmann approach shows significant deviations in this regime. However, for transport described by (45)–(47), the transport coefficients are relatively small in this regime and their utility and accuracy are not of paramount importance. We have defined the onset of the caged regime as the point at which the first oscillation in the VACF becomes negative and an approximate representation of this boundary in the range $\kappa \in [0,2]$ is given by

$$\Gamma_{\rm cage} \approx 34.1 + 17.1\kappa^2 - 13.6\kappa^3 + 5.39\kappa^4. \tag{85}$$

Next, in Fig. 16 we examine the same properties in more detail to reveal additional ways in which the Boltzmann picture begins to fail. Here we show the VACF itself as a function of

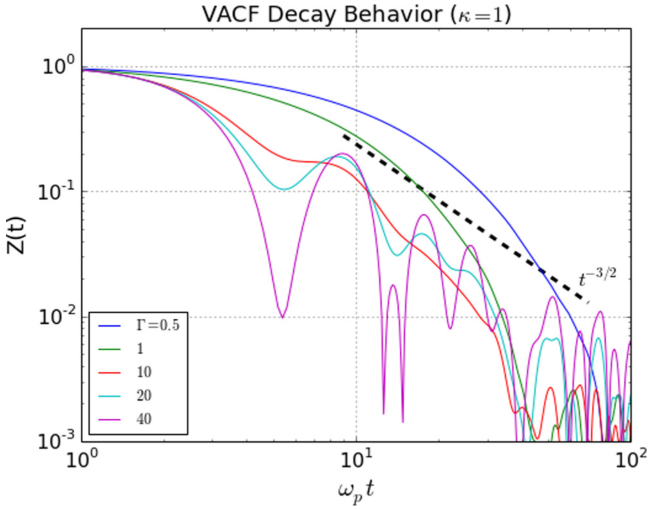

FIG. 16. Transition from exponential decay to algebraic $t^{-3/2}$ decay versus coupling. Several VACFs on a log-log scale are shown for fixed $\kappa = 1$ and various values of Γ. Note that the top two curves show exponential decay and this decay is faster than the dashed $t^{-3/2}$ line. However, near $\Gamma \sim 10$, the decay remains mostly exponential but with important modulations at later times. At $\Gamma = 20$, the VACF has well-defined minima and decays very slowly at late time, a behavior that increases for large Γ.

time for several values of Γ and, without loss of generality, for fixed $\kappa = 1$. Note that this plot is on a log-log scale in which power laws appear as straight lines. The top two curves (blue and green) decay exponentially for small Γ, consistent with the Boltzmann picture. However, for $\Gamma \gtrsim 10$, the decay not only exhibits inflections but also begins to form a slowly decaying tail. This tail broadens as the coupling increases. We also show a dashed line consistent with a decay of $\sim 1/t^{3/2}$, which is the the so-called long-time tail [82]. Our results indicate a transition to the long-time tail around $\Gamma \gtrsim 10$, but always in the presence of oscillations.

While the interaction within the EB formalism is inherently static, it is possible to modify the effective screening length to incorporate finite-velocity effects. The effective interactions between ions will become more Coulomb-like at higher velocities, as the screening background is unable to respond as quickly. Zwicknagel *et al.* [83] suggested the following form to modify the ionic screening length:

$$\lambda_i(v) = \left[1 + \left(\frac{v}{v_i}\right)^2\right]^{1/2} \lambda_i, \tag{86}$$

where we have defined the thermal velocity of the ith species as $v_i = (2T/m_i)^{1/2}$, although this is not a unique choice. As shown by Grabowski *et al.* [27], the modification (86) yields surprisingly good agreement when predicting dynamical properties such as stopping power. The resulting velocity-dependent effective screening length will then take the form

$$\lambda_{\text{eff}}(v) = \left[\frac{1}{\lambda_e^2} + \sum_i \frac{1}{\lambda_i^2}\left(\frac{1}{1 + v^2/v_i^2 + 3\Gamma_i}\right)\right]^{-1/2}. \tag{87}$$

It is important to note that this quantity can no longer be applied to the fits (C22)–(C24) and must instead be used in the momentum-transfer cross sections first before calculating the collision integrals due to the velocity dependence. We examine the implications of a velocity-dependent screening length in Fig. 17, where we show the ratio of the dynamically screened cross section using (87) and its static counterpart [i.e., $\lambda_{\text{eff}}(v = 0)$] as a function of v/v_i for a range of Γ. One expects the dynamical effects to be negligible at low velocities; however, these effects are small at high velocities as well. This latter behavior occurs because the screening length itself has little impact on the cross section in this regime. Indeed, it is only when $v \sim v_i$ that dynamical effects are greatest and these effects on the cross section are greater for larger coupling values.

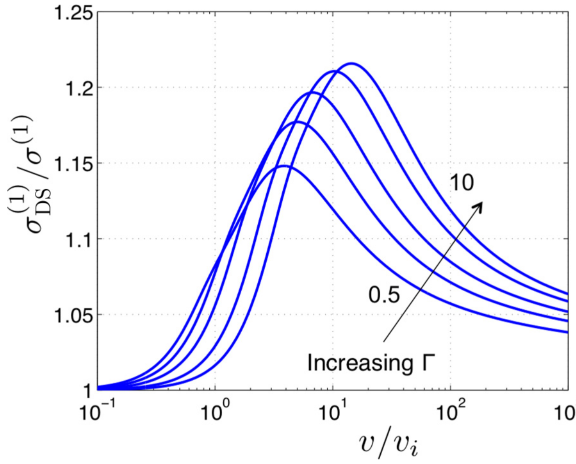

FIG. 17. Impact of a velocity-dependent screening length $\lambda(v)$ on the first-order cross section shown by taking the ratio of the dynamically screened cross section using $\lambda_{\text{eff}}(v)$ (denoted by $\sigma^{(1)}_{\text{DS}}$) to that using only the static λ_{eff} as a function of v/v_i. The results are calculated at $\kappa = 0.5$ for the values $\Gamma = \{0.5,1,2,5,10\}$. Deviations are greatest for $v \sim v_i$ and increase for larger coupling values.

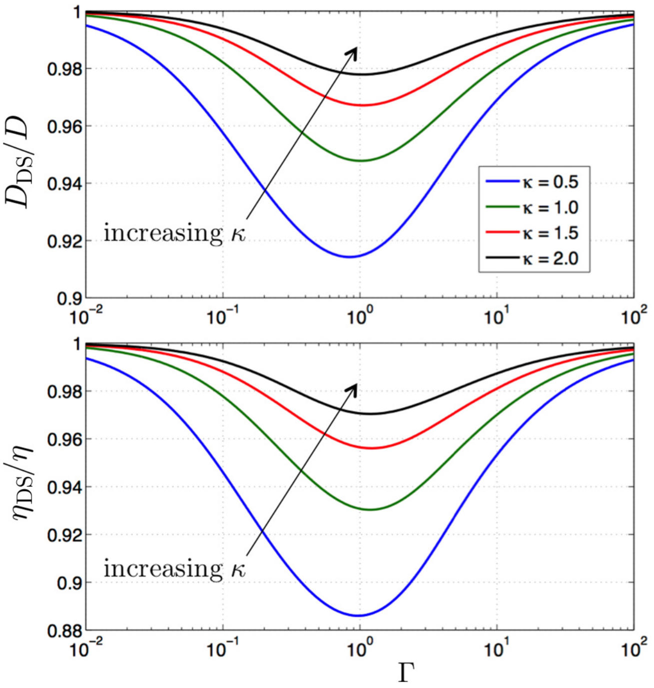

FIG. 18. Ratio of the dynamically screened self-diffusion (top) and viscosity (bottom) coefficients to their static counterparts as a function of coupling Γ for $\kappa = \{0.5,1,1.5,2\}$. Note that for weaker screening (smaller κ), the dynamical correction can be significant.

Once the momentum-transfer cross sections are computed with (87), the collision integrals can be recalculated to determine the effects of dynamic screening on the transport coefficients. In Fig. 18 we show the ratios of the dynamically screened self-diffusion and viscosity to their static counterparts. As we can see, dynamic screening can reduce each coefficient on the order of 10% when $\Gamma \sim 1$ and κ is small. However, for systems with strong electron screening (large κ), the effects of dynamic ion screening are negligible for all coupling strengths.

VII. CONCLUSION AND OUTLOOK

Ionic transport in dense HED plasmas, including self-diffusion, interdiffusion, viscosity, and thermal conductivity, has been described using an effective potential approach in the context of the CE solution of the Boltzmann equation. We have focused on the weak-screening and moderate-coupling regimes where transport can play an important role in HED experiments. For practical use, we have formulated an effective potential that is of the screened Coulomb (Yukawa) form, which allows detailed numerical solutions to be reduced

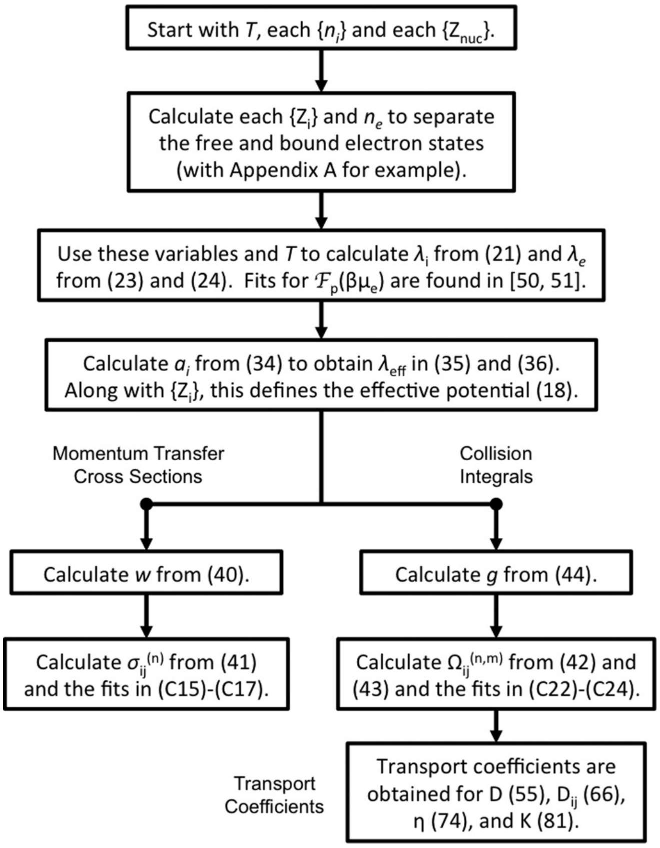

FIG. 19. Diagram outlining the algorithm to calculate transport properties using the fits of this work. The calculation begins with a determination of the atomic structure of the possibly partially ionized mixture, followed by a determination of the relevant plasma properties (electron screening length and ion screening length) to obtain the effective screening length. This can then be used to compute transport coefficients either near equilibrium (right branch) or using cross sections and a non-Maxwellian distribution (left branch).

to simple fits valid over wide ranges of parameter values. Fits have been provided for both the intermediate velocity-dependent cross sections and the thermally averaged collision integrals, allowing one to easily obtain the near-equilibrium ionic transport coefficients or perform integrals over the cross section weighted by a non-Maxwellian distribution. Our approach has greatly extended the numerical methods needed to compute the collision integrals and our results are more accurate over a wider range of parameter values and considerably simpler to use than those of Paquette *et al.* [5]. A brief overview of how our results can be used to model HED plasmas is shown in the diagram in Fig. 19. In our analysis, we have also connected the effective Boltzmann approach to the simpler CL approach and have detailed the natures of the approximations that are required to obtain specific CL models. Interestingly, while there is a convergence of the EB approach to the simpler CL models at weaker coupling, we find that the convergence is extremely slow and poorly behaved, as shown in Fig. 4.

We have validated our results with MD simulations for the self-diffusion coefficient and found the EB model to be quite predictive over the ranges of Γ and κ of importance to HED experiments, thereby validating our model for the effective potential. In particular, we found that the effective screening length (28) yields excellent agreement between the theoretical model and MD results. We have also compared our predictions for the other transport coefficients to MD results from the literature and have found similarly good agreement in the weak- to moderate-coupling regimes where the coefficients are large. As expected, the EB approach deviates from the MD results at larger coupling and for certain coefficients (i.e., η and K), the EB model is unable to predict their respective minima; however, this regime is difficult to achieve experimentally and the coefficients are near their minimum values in this regime as well.

We have also explored the limitations of the EB approach in detail. The behavior of the VACF was examined across the liquid portion of the Yukawa phase diagram in the (Γ,κ) space. We have delineated several regimes wherein the VACF exhibits qualitatively different behaviors. In the first regime, the decay of the VACF is close to exponential (defined as purely monotonic) and the Boltzmann equation would be a reasonable approximation. In the next regime, the decay was modulated but always positive, and in the final regime, caging (anticorrelations in the velocity) was observed. In fact, many other types of behavior are possible (e.g., the first minimum is positive, but the second is not); however, these possibilities are beyond the scope of this work. Surprisingly, the EB model performs well in much of the modulated decay region despite being unable to capture the presence of these modulations. Next, we also examined the assumption of static screening in the effective potential. Because the velocity of the ions will be distributed well below, near, and well above the thermal velocity, dynamical screening could play a role. Using an effective, velocity-dependent screening length that has been shown to be very successful for stopping power [27], we found small ($\sim$10%) changes in the transport coefficients, suggesting that the use of the static, effective screening lengths in (28) is justified to that level of accuracy.

This work can be extended in several ways. First, other ionic transport coefficients, such as those for thermal diffusion and mixture viscosities [47], could be considered. Second, the EB model and our extension to include velocity-dependent screening could be examined with LB approaches, in which the dynamical long-range screening is treated more rigorously. Third, we have not treated the various transport processes that involve electron scattering, such as thermal conductivity and electron-ion temperature relaxation, as in (47) and (80); such scattering requires a quantum treatment.

ACKNOWLEDGMENTS

This work was performed under the auspices of the U.S. Department of Energy by Lawrence Livermore National Laboratory under Contract No. DE-AC52-07NA27344 and by Los Alamos National Laboratory under Contract No. DE-AC52-06NA25396. The authors would like to thank Lisa Murillo for her detailed editing of the document, Julie Stern for her early contributions to this work, and William Cabot, Jeff Greenough, Jeff Haack, and George Zimmerman for very useful feedback on the manuscript. This document is LA-UR-16-20725 (LANL) and LLNL-JRNL-681618 (LLNL).

APPENDIX A: MEAN IONIZATION STATES IN PARTIALLY IONIZED MIXTURES

In our effective potential approach, the effective screening length λ_{eff} plays a central role; however, another key input is the ionic charge. Throughout this work, the quantity $Z_i e$ represents either the nuclear charge in a fully ionized plasma or the mean ionization state (MIS) in a partially ionized plasma. In the latter case, an ionization model is required to appropriately separate free electrons that weakly interact with the nuclei and those with strong interactions that are bound. By doing so, the strongly interacting bound states are treated as a compact charge density near the nucleus, while the remaining free states are treated using an appropriate linear screening model [54].

A wide range of MIS models has been developed and detailed comparisons among many of these models can be found in [84]. The simplest model that includes both thermal and pressure ionization is the so-called Thomas-Fermi model, first developed by Feynman *et al.* [85], which can be readily implemented as an average atom model where the electronic structure $n_e(r)$ about a single central nucleus in a charge-neutral spherical cell is calculated for a particular ionic number density and temperature. The effects of ionic density, such as pressure ionization, enter through the choice of the radius of the cell as a_i. The MIS can be defined in terms of the value of the normalized electron density evaluated at the ion-sphere radius $Z_{\text{TF}} = Z_{\text{nuc}} - \frac{4}{3}\pi a_i^3 n_e(a_i)$, where Z_{nuc} is the bare nuclear charge. Despite its facile prescription, this TF model can be fairly accurate over a wide range of parameters [84].

To avoid the expense of computing the atomic structure within a hydrodynamics code, an approximate fit to the function $Z_{\text{TF}}(n_i, Z_{\text{nuc}}, T_e)$ was given in [86], which we repeat for convenience and completeness in Table II. In comparison with the original description [86], we have simplified the implementation of the fit by only requiring the ionic number density rather than both the mass density and atomic mass of the species.

The TF model has the additional advantage of being fairly straightforward to implement in multicomponent systems. Using reasoning similar to that used in Sec. III B, the MIS of each species must be calculated as $Z_i = Z_{\text{TF}}(V_i^{-1}, Z_{\text{nuc},i}, T_e)$, where V_i is the volume of the ion sphere associated with the ith species in the presence of the other species. To calculate each reduced volume, we set $V_i/Z_i = V_j/Z_j$ for every pair of species; this is consistent with the TF model of [85], which assumed that the free-electron density is uniform beyond the ion sphere. Finally, the volumetric constraint of $\sum_i n_i V_i = 1$ is required for completeness. As an example, a two-component system would require the solution of the equations

$$Z_1 = Z_{\text{TF}}\big(V_1^{-1}, Z_{\text{nuc},1}, T_e\big), \tag{A1}$$

$$Z_2 = Z_{\text{TF}}\big(V_2^{-1}, Z_{\text{nuc},2}, T_e\big), \tag{A2}$$

$$n_1 V_1 + n_2 V_2 = 1, \quad \frac{V_1}{Z_1} = \frac{V_2}{Z_2}. \tag{A3}$$

Simple iterative methods can be used to rapidly converge to a solution of this system.

TABLE II. Fit and coefficients from [86] for the Thomas-Fermi mean-ionization model. The Avogadro constant is $N_A = 6.022\,14 \times 10^{23}$, Z_{nuc} is the nuclear charge number, the ionic number density n_i is in units of $1/\text{cm}^3$, and the electron temperature is in units of eV.

$\alpha_1 = 14.3139$	$\alpha_2 = 0.6624$
$R = n_i / Z_{\text{nuc}} N_A$	$k_0 = 3.323 \times 10^{-3}$
$T_0 = T_e Z_{\text{nuc}}^{-4/3}$	$k_1 = 0.9718$
$T_f = T_0/(1 + T_0)$	$k_2 = 9.26148 \times 10^{-5}$
$A = k_0 T_0^{k_1} + k_2 T_0^{k_3}$	$k_3 = 3.10165$
$B = -\exp(k_4 + k_5 T_f + k_6 T_f^7)$	$k_4 = -1.7630$
$C = k_7 T_f + k_8$	$k_5 = 1.43175$
$Q_1 = A R^B$	$k_6 = 0.31546$
$Q = (R^C + Q_1^C)^{1/C}$	$k_7 = -0.366667$
$x = \alpha_1 Q^{\alpha_2}$	$k_8 = 0.983333$
$Z_{\text{TF}} = Z_{\text{nuc}} x/(1 + x + \sqrt{1 + 2x})$	

APPENDIX B: TRANSPORT COEFFICIENTS

The plasma transport coefficients can be derived using a variety of methods and here we provide a more detailed background for the approach we employ. In this work we base our results on an effective Boltzmann approach [27,28,34,40], in which we build upon the Boltzmann equation, which includes strong scattering through a numerical cross section, by capturing long-range screening effects through an effective potential to incorporate both branches of kinetic theory shown in Fig. 1. Such an approach yields a convergent kinetic model for all of the transport coefficients needed in a hydrodynamic description of a dense plasma.

The effective Boltzmann approach is described through a set of coupled Boltzmann equations for each species j of the form

$$\frac{\partial}{\partial t} f_j + \mathbf{v} \cdot \nabla f_j + \frac{\mathbf{F}_j^{\text{ext}}}{m_j} \cdot \nabla f_j = \sum_l C_{jl}[f_j, f_l], \tag{B1}$$

$$C_{jl}[f_j, f_l] = \iint d\mathbf{v}' d\Omega\, g I(g,\theta)(f_j' f_l' - f_j f_l). \tag{B2}$$

Here $\mathbf{F}_j^{\text{ext}}$ is any external force, $g = |\mathbf{v} - \mathbf{v}'|$ is the relative velocity, Ω is the solid angle, the primes denote functions of $\mathbf{v}'$, and the differential cross section is defined as

$$I(g,\theta) = \frac{b}{\sin(\theta)} \frac{db}{d\theta}. \tag{B3}$$

As we detail in Sec. VI, such a kinetic model makes several assumptions. While strong scattering is well described through the cross section (B3), the cross section is only a well-defined quantity for binary collisions in which the initial and final states are distinct and separated, as in (B2); note that the time evolution of the scattering event does not appear in Boltzmann descriptions. For example, if $\mathbf{F}_j^{\text{ext}}$ were to include a Vlasov contribution, the resulting dynamical fluctuations could not modify (B3) in any simple way, as is also discussed in Sec. VI.

As written for Coulomb systems, (B1) is famously divergent; this difficulty is eased via the use of an effective potential, as in (18). The cross section in this effective potential is obtained from (3) and (5). Given this scheme, the relevant coefficients remain to be generated. The standard procedure

[47] is the CE expansion, which yields a solution of (B1) that can be used to construct hydrodynamic moments and, importantly, closed-form expressions for the fluxes associated with these moments. This method proceeds by using a method of successive approximations for the distribution functions f_j,

$$f_j = \frac{1}{\epsilon} f_j^{(0)} + f_j^{(1)} + \epsilon f_j^{(2)} + \cdots , \tag{B4}$$

where ϵ is an ordering parameter. The lowest-order solution $f^{(0)}$ can be shown to be a local drifting Maxwellian. In turn, higher-order corrections can be systematically obtained by substituting the full CE expansion (B4) into the Boltzmann equations (B1). From the relevant fluxes computed using the solution (B4), leading-order expressions for the transport coefficients can be obtained. For transport processes associated with single-component systems, we have

$$D = \frac{3T}{8nm_i\Omega_{ii}^{(11)}}, \tag{B5}$$

$$\eta = \frac{5T}{8\Omega_{ii}^{(22)}}, \tag{B6}$$

$$K = \frac{75T}{32m_i\Omega_{ii}^{(22)}}, \tag{B7}$$

which are the self-diffusivity, viscosity, and thermal conductivity, respectively. For transport processes associated with systems of multiple components, the coefficients become increasingly complicated, as a linear set of equations must be inverted. In a binary mixture, we have

$$D_{ij} = \frac{3T}{16n\mu_{ij}\Omega_{ij}^{(11)}}, \tag{B8}$$

$$\eta_{\text{tot}} = \frac{x_i^2\mathcal{R}_i + x_j^2\mathcal{R}_j + x_ix_j\mathcal{R}'_{ij}}{x_i^2\mathcal{R}_i\eta_i^{-1} + x_j^2\mathcal{R}_j\eta_j^{-1} + x_ix_j\mathcal{R}_{ij}}, \tag{B9}$$

$$K_{\text{tot}} = \frac{x_i^2\mathcal{Q}_iK_i + x_j^2\mathcal{Q}_jK_j + x_ix_j\mathcal{Q}'_{ij}}{x_i^2\mathcal{Q}_i + x_j^2\mathcal{Q}_j + x_ix_j\mathcal{Q}_{ij}}, \tag{B10}$$

$$k_T \equiv \frac{D_T}{D_{ij}} = \frac{5x_ix_j\mathcal{C}(x_i\mathcal{S}_i - x_j\mathcal{S}_j)}{x_i^2\mathcal{Q}_i + x_j^2\mathcal{Q}_j + x_ix_j\mathcal{Q}_{ij}}, \tag{B11}$$

with the coefficients

$$\mathcal{A} = \frac{\Omega_{ij}^{(22)}}{5\Omega_{ij}^{(11)}}, \quad \mathcal{B} = \frac{5\Omega_{ij}^{(12)} - \Omega_{ij}^{(13)}}{5\Omega_{ij}^{(11)}}, \quad \mathcal{C} = \frac{2\Omega_{ij}^{(12)}}{5\Omega_{ij}^{(11)}} - 1, \quad \mathcal{E} = \frac{T}{8M_iM_j\Omega_{ij}^{(11)}}, \tag{B12}$$

$$\mathcal{P}_i = \frac{M_i}{\eta_i}\mathcal{E} = \frac{\Omega_{ii}^{(22)}}{5M_j\Omega_{ij}^{(11)}}, \quad \mathcal{P}_{ij} = 3(M_i - M_j)^2 + 4M_iM_j\mathcal{A}, \tag{B13}$$

$$\mathcal{Q}_i = \mathcal{P}_i\big(6M_j^2 + 5M_i^2 - 4M_i^2\mathcal{B} + 8M_iM_j\mathcal{A}\big), \quad \mathcal{Q}'_{ij} = \frac{15\mathcal{E}[\mathcal{P}_i + \mathcal{P}_j + (11 - 4\mathcal{B} - 8\mathcal{A})M_iM_j]}{2(m_i + m_j)}, \tag{B14}$$

$$\mathcal{Q}_{ij} = 2\mathcal{P}_i\mathcal{P}_j + 3(M_i - M_j)^2(5 - 4\mathcal{B}) + 4M_iM_j\mathcal{A}(11 - 4\mathcal{B}), \quad \mathcal{R}_i = \frac{2}{3} + \frac{M_i}{M_j}\mathcal{A}, \tag{B15}$$

$$\mathcal{R}_{ij} = \frac{4\mathcal{A}}{3M_iM_j\mathcal{E}} + \frac{\mathcal{E}}{2\eta_i\eta_j}, \quad \mathcal{R}'_{ij} = \frac{4}{3} + \frac{\mathcal{E}}{2\eta_i} + \frac{\mathcal{E}}{2\eta_j} - 2\mathcal{A}, \quad \mathcal{S}_i = M_i\mathcal{P}_i - M_j[3(M_j - M_i) + 4M_i\mathcal{A}], \tag{B16}$$

where the mass ratios are $M_i = m_i/(m_i + m_j)$ and the number density ratios are $x_i = n_i/(n_i + n_j)$ [47]. Here the coefficients D_{ij}, η_{tot}, K_{tot}, and k_T are the interdiffusivity, total viscosity, total thermal conductivity, and thermal diffusion ratio, which is the ratio of the thermal diffusion coefficient D_T to the interdiffusivity. Higher-order corrections can also be obtained (see, e.g., [33,47]), but they are usually very small.

The general problem of transport is made complex by the introduction of both more complex phenomena and mixtures [87,88]. In the former category, plasmas may contain magnetic fields, electric fields [10], gravitational fields, relativity, radiation, multiple ionization states, multiple temperatures, and so on. For example, sedimentation in white dwarfs [89] and neutron stars [90] involves impurities in strongly coupled mixtures in electric and gravitational fields; in fact, the structure of the flux equations, as in (62), has coupling corrections beyond what appear in the transport coefficients themselves [90,91]. Mixtures cause additional complexities due to couplings among the various continuity and momentum equations, which require potentially large matrix inversions [92–96]. It is thus impossible to express generalized coefficients without specifying the physical model; however, in most cases the transport equations are formulated in terms of the binary coefficients we present here.

APPENDIX C: NUMERICAL EVALUATION OF INTEGRALS

To reduce the dimension of parameter space, it is useful to nondimensionalize the spatial scale of the problem. While several length scales are present, the ideal choice is the screening length λ, as it does not contain any variables of integration (e.g., the impact parameter). We therefore introduce the dimensionless parameters

$$r \rightarrow \lambda r, \quad \rho = \frac{b}{\lambda}, \quad w^2 = \frac{\mu\lambda}{2Z_iZ_je^2}v^2, \tag{C1}$$

where we have assumed a finite value for λ. In the case $\lambda = 0$, there is no interaction and thus the trivial result $\theta_{ij} = \sigma_{ij}^{(k)} = \Omega_{ij}^{(k,l)} = 0$ is obtained. Alternatively, as $\lambda \to \infty$, we recover the Coulomb interaction, which yields the scattering angle (8). The corresponding momentum-transfer cross sections will diverge as $b \to \infty$; however, truncating this upper limit with the screening length yields the finite forms (9) and (10).

1. Scattering-angle integral

In the transformed variables (C1), the scattering angle takes the form

$$\theta_{ij}(\rho,w) = \pi - 2\rho \int_{r_0}^{\infty} \frac{r^{-1}dr}{\sqrt{r^2 - \rho^2 - w^{-2}re^{-r}}}, \tag{C2}$$

where r_0 still satisfies the the zero of the denominator. This integral is improper because of both this singularity at the lower limit and the infinite upper limit. We wish to circumvent these issues for numerical reasons and thus introduce the variable $s = (1 - r_0/r)^{1/4}$ to yield

$$\theta_{ij}(\rho,w) = \pi - \int_0^1 \frac{8\gamma s^3 ds}{\sqrt{1 - \gamma^2(1-s^4)^2 - u(s)}}, \tag{C3}$$

$$u(s) = \frac{1-s^4}{w^2 r_0} \exp\left(\frac{-r_0}{1-s^4}\right), \quad \gamma = \sqrt{1 - \frac{e^{-r_0}}{w^2 r_0}}. \tag{C4}$$

We can examine the large-angle scattering limit by approximating $u(s) \approx u_0(s) = (1-s^4)e^{-r_0}/w^2 r_0$, which gives the scattering angle

$$\theta_0(\gamma) = \pi + 2\sin^{-1}\left(\frac{\gamma^2 - 1}{\gamma^2 + 1}\right). \tag{C5}$$

Adding and subtracting this limiting solution to (C2) yields the more rapidly converging integral

$$\begin{aligned}\theta_{ij}(\rho,w) = &\int_0^1 \frac{8\gamma s^3 ds}{\sqrt{1 - \gamma^2(1-s^4)^2 - u_0(s)}} \\ &- \int_0^1 \frac{8\gamma s^3 ds}{\sqrt{1 - \gamma^2(1-s^4)^2 - u(s)}} \\ &- 2\sin^{-1}\left(\frac{\gamma^2-1}{\gamma^2+1}\right).\end{aligned} \tag{C6}$$

Given the broad range of parameters, we used an adaptive integration scheme in which quadrature points were doubled upon each iteration until the desired convergence was achieved. The treatment of the distance of closest approach r_0 will be addressed in the next subsection.

2. Cross-section integrals

The momentum-transfer cross sections now take the form

$$\sigma_{ij}^{(n)}(w,\lambda) = 2\pi\lambda^2 \phi_n(w), \tag{C7}$$

$$\phi_n(w) = \int_0^{\infty} d\rho\, \rho\{1 - \cos^n[\theta_{ij}(\rho,w)]\}. \tag{C8}$$

To integrate over ρ, we must continually calculate the distance of closest approach r_0 from the implicit relation $r_0^2 = \rho^2 + r_0 e^{-r_0}/w^2$. We can simplify the parameter space by first writing $\rho = \rho(r_0,w)$ and introducing the integration variable $z = (r_0 - r_c)^{1/p}$, where r_c is defined through the simpler implicit relation $r_c = e^{-r_c}/w^2$ and the parameter p can be changed depending on the stiffness of the integrand. Equation (C8) can now be written as

$$\phi_n(w) = p\int_0^{\infty} dz\, z^{p-1} f(z,r_c)[1 - \cos^n(\theta_{ij})], \tag{C9}$$

with

$$f(z,r_c) = z^p + r_c + \frac{z^p + r_c - 1}{2w^2 \exp(z^p + r_c)}. \tag{C10}$$

While the upper bound is still infinite, the integrand was found to decay sufficiently fast enough to allow for a truncated domain. As with (C6), we employed a similar adaptive integration scheme.

It can be shown that $\phi_n(w)$ will take on asymptotic forms

$$\phi_n(w) \sim \frac{n}{w^4} \ln(w) \tag{C11}$$

for $w \gg 1$ and

$$\phi_n(w) \sim \mathcal{A}_n \ln^2(w^2) + \mathcal{A}_n' \ln(w^2) + \mathcal{A}_n'' \tag{C12}$$

for $w \ll 1$. The values of the above coefficients for the low-w limit were found numerically to be

$$\mathcal{A}_1 = 0.47871, \quad \mathcal{A}_1' = 2.7935, \quad \mathcal{A}_1'' = 15.944, \tag{C13}$$

$$\mathcal{A}_2 = 0.32020, \quad \mathcal{A}_2' = 1.0479, \quad \mathcal{A}_2'' = 7.8182. \tag{C14}$$

With these asymptotic forms in mind, we have constructed a suitable fit that obeys each limit, respectively:

$$\phi_n(w) \approx \begin{cases} \phi_n^{\mathrm{SC}}(w), & w < 1 \\ \phi_n^{\mathrm{WC}}(w), & w > 1, \end{cases} \tag{C15}$$

where the strongly coupled component is given by

$$\phi_n^{\mathrm{SC}}(w) = \frac{c_0 + c_1\ln(w) + c_2\ln^2(y) + c_3\ln^3(w)}{1 + c_4\ln(w)} \tag{C16}$$

TABLE III. Coefficients for fits (C16)–(C18) of the reduced cross sections (C8).

n	c_0	c_1	c_2	c_3	c_4	d_0	d_1	d_2	d_3	d_4	d_5
1	0.30031	−0.69161	0.59607	−0.39822	−0.20685	0.48516	1.66045	−0.88687	0.55990	1.65798	−1.02457
2	0.40688	−0.86425	0.77461	−0.34471	−0.27626	0.83061	1.05229	−0.59902	1.41500	0.78874	−0.48155

TABLE IV. Coefficients for fits (C23)–(C24) of the reduced collision integrals.

(n,m)	a_1	a_2	a_3	a_4	a_5	b_0	b_1	b_2	b_3	b_4
(1,1)	1.4660	−1.7836	1.4313	−0.55833	0.061162	0.081033	−0.091336	0.051760	−0.50026	0.17044
(1,2)	0.52094	0.25153	−1.1337	1.2155	−0.43784	0.20572	−0.16536	0.061572	−0.12770	0.066993
(1,3)	0.30346	0.23739	−0.62167	0.56110	−0.18046	0.68375	−0.38459	0.10711	0.10649	0.028760
(2,2)	0.85401	−0.22898	−0.60059	0.80591	−0.30555	0.43475	−0.21147	0.11116	0.19665	0.15195

and the weakly coupled component is given by

$$\phi_n^{\mathrm{WC}}(w) = \frac{n}{2w^4}\ln(1+w^2)P(w), \tag{C17}$$

$$P(w) = \left[\frac{d_0 + d_1\ln(w) + d_2\ln^2(w) + \ln^3(w)}{d_3 + d_4\ln(w) + d_5\ln^2(w) + \ln^3(w)}\right]. \tag{C18}$$

By next minimizing the magnitude of the relative error between the fit and the numerical calculations while still maintaining $\mathcal{C}^1$ continuity of the overall function (particularly at $w = 1$), we have obtained values of these coefficients for which maximal deviations from (C8) are on the order of 10^{-3} near $w \approx 16$ (but are usually under 10^{-5}). The coefficients for (C16) and (C18) are presented for $n = \{1,2\}$ in Table III.

3. Collision integrals

Finally, we turn to the collision integral expressed in terms of the transformed variables as

$$\Omega_{ij}^{(n,m)} = \sqrt{\frac{2\pi}{\mu_{ij}}}\frac{(Z_iZ_je^2)^2}{T^{3/2}}\mathcal{K}_{nm}(g), \tag{C19}$$

$$\mathcal{K}_{nm}(g) \equiv g^m\int_0^\infty dw\, e^{-gw^2}w^{2m+3}\phi_n(w), \tag{C20}$$

where

$$g = \frac{Z_iZ_je^2}{\lambda T}. \tag{C21}$$

The integration of (C20) was performed over three intervals, where an intermediate range of $w \in [10^{-7},10^2]$ used numerically calculated values of $\phi_n(w)$ with cubic spline interpolation and asymptotic limits of $\phi_n(w)$ were used outside this range. Once $\mathcal{K}_{nm}(g)$ was calculated for each index pair (n,m), the numerical values were used to generate fitting functions. For optimal accuracy, we divide these fits into two regions as

$$\mathcal{K}_{nm}(g) \approx \begin{cases} \mathcal{K}_{nm}^{\mathrm{WC}}(g), & g < 1 \\ \mathcal{K}_{nm}^{\mathrm{SC}}(g), & g > 1, \end{cases} \tag{C22}$$

where the weakly coupled component is given by

$$\mathcal{K}_{nm}^{\mathrm{WC}}(g) = -\frac{n}{4}(m-1)!\ln\left(\sum_{k=1}^{5}a_kg^k\right) \tag{C23}$$

and the strongly coupled component is given by

$$\mathcal{K}_{nm}^{\mathrm{SC}}(g) = \frac{b_0 + b_1\ln(g) + b_2\ln^2(g)}{1 + b_3g + b_4g^2}. \tag{C24}$$

As with (C15)–(C18), the coefficients were determined by minimizing the magnitude of the relative difference between the fit and the numerical calculations while maintaining $\mathcal{C}^1$ continuity of the overall function (particularly at $g = 1$). This optimization yields deviations from (C20) on the order of 10^{-2}, where these deviations are maximized around $g \approx 2$, and the coefficient values are presented in Table IV for the (n,m) pairs relevant to first-order CE theory.

---

[1] A. Bobylev, A. Brantov, V. Bychenko, S. Karpov, and I. Potapenko, Acta Appl. Math. **132**, 107 (2014).

[2] M. S. Rosin, L. F. Ricketson, A. M. Dimits, R. E. Caflish, and B. I. Cohen, J. Comput. Phys. **274**, 140 (2014).

[3] A. M. Dimits, C. Wang, R. Caflish, B. I. Cohen, and Y. Huang, J. Comput. Phys. **228**, 4881 (2009).

[4] M. Giersz, D. C. Heggie, and J. R. Hurley, Mon. Not. R. Astron. Soc. **388**, 429 (2008).

[5] C. Paquette, C. Pelletier, G. Fontaine, and G. Michaud, Astron. J. Suppl. Ser. **61**, 177 (1986).

[6] S. A. Khrapak, A. V. Ivlev, G. E. Morfill, and H. M. Thomas, Phys. Rev. E **66**, 046414 (2002).

[7] J. Castro, P. McQuillen, H. Gao, and T. C. Killian, J. Phys.: Conf. Ser. **194**, 012065 (2009).

[8] T. Pohl, T. Pattard, and J. M. Rost, J. Phys. B **38**, S343 (2005).

[9] A. E. Turrell, M. Sherlock, and S. J. Rose, J. Comput. Phys. **299**, 144 (2015).

[10] P. Amendt, O. L. Landen, H. F. Robey, C. K. Li, and R. D. Petrasso, Phys. Rev. Lett. **105**, 115005 (2010).

[11] C. R. Weber, D. S. Clark, A. W. Cook, L. E. Busby, and H. F. Robey, Phys. Rev. E **89**, 053106 (2014).

[12] B. M. Haines, E. L. Vold, and K. Moldwig, Phys. Plasmas **21**, 092306 (2014).

[13] C. K. Li and R. D. Petrasso, Phys. Rev. Lett. **70**, 3063 (1993).

[14] C. K. Li and R. D. Petrasso, Phys. Rev. Lett. **70**, 3059 (1993).

[15] L. Jiang and H.-L. Tsai, J. Appl. Phys. **104**, 093101 (2008).

[16] D. Comparat, T. Vogt, N. Zahzam, M. Mudrich, and P. Pillet, Mon. Not. R. Astron. Soc. **361**, 1227 (2005).

[17] P. Debye and E. Hückel, Phys. Z. **24**, 185 (1923).

[18] D. Pines and D. Bohm, Phys. Rev. **85**, 338 (1952).

[19] L. Landau, Phys. Z. Sowjetunion **10**, 154 (1936).

[20] J. Yvon, *La Théorie Statistique des Fluides et l'Équation d'État*, Actualités Scientifiques et Industrielles No. 203 (Hermann, Paris, 1935); M. Born and H. S. Green, Proc. R. Soc. London

Ser. A **188**, 10 (1946); J. G. Kirkwood, J. Chem. Phys. **14**, 180 (1946); N. N. Bogoliubov, Zh. Eksp. Teor. Fiz. **16**, 691 (1946).

[21] R. L. Liboff, *Kinetic Theory: Classical, Quantum, and Relativistic Descriptions* (Springer, Berlin, 2003).

[22] A. Lenard, Ann. Phys. (N.Y.) **10**, 390 (1960).

[23] Balescu, Phys. Fluids **3**, 52 (1960).

[24] It should be noted that although quantum Lenard-Balescu formulations are convergent as a result of a natural b_{min} cutoff near the thermal de Broglie wavelength, the true cutoff arising from strong scattering may be missed with this formulation. Lenard-Balescu formulations that employ an effective potential including a local-field correction can more accurately incorporate such cutoffs.

[25] J. N. Glosli, F. R. Graziani, R. M. More, M. S. Murillo, F. H. Streitz, M. P. Surh, L. X. Benedict, S. Hau-Riege, A. B. Langdon, and R. A. London, Phys. Rev. E **78**, 025401(R) (2008).

[26] Q. Ma, J. Dai, D. Kang, J. Yuan, and X. Zhao, High Energy Density Phys. **13**, 34 (2014).

[27] P. E. Grabowski, M. P. Surh, D. F. Richards, F. R. Graziani, and M. S. Murillo, Phys. Rev. Lett. **111**, 215002 (2013).

[28] R. L. Liboff, Phys. Fluids **2**, 40 (1959).

[29] T. Kihara, J. Phys. Soc. Jpn. **14**, 402 (1959).

[30] J. G. Kirkwood, J. Chem. Phys. **3**, 300 (1935).

[31] B. Roux, Comput. Phys. Commun. **91**, 275 (1995).

[32] D. Chandler, *Introduction to Modern Statistical Mechanics* (Oxford University Press, New York, 1987).

[33] D. A. McQuarrie, *Statistical Mechanics* (University Science Books, South Orange, 2000).

[34] O. Aono, J. Phys. Soc. Jpn. **17**, 853 (1962).

[35] E. A. Frieman and D. L. Book, Phys. Fluids **6**, 1700 (1963).

[36] T. Kihara and O. Aono, J. Phys. Soc. Jpn. **18**, 837 (1963).

[37] H. A. Gould and H. E. DeWitt, Phys. Rev. **155**, 68 (1967).

[38] L. S. Brown, D. L. Preston, and R. L. Singleton, Phys. Rev. E **86**, 016406 (2012).

[39] D. Muchmore, Astrophys. J. **278**, 769 (1984).

[40] D. O. Gericke, M. S. Murillo, and M. Schlanges, Phys. Rev. E **65**, 036418 (2002).

[41] S. Chandrasekhar, Astrophys. J. **97**, 255 (1943).

[42] R. S. Cohen, L. Spitzer, and P. Routly, Phys. Rev. **80**, 230 (1950).

[43] M. N. Rosenbluth, W. M. MacDonald, and D. L. Judd, Phys. Rev. **107**, 1 (1957).

[44] S. Ichimaru, H. Iyetomi, and S. Tanaka, Phys. Rep. **149**, 91 (1987).

[45] S. Tanaka and S. Ichimaru, Phys. Rev. A **34**, 4163 (1986).

[46] S. A. Khrapak, Phys. Plasmas **20**, 054501 (2013).

[47] S. Chapman and T. G. Cowling, *The Mathematical Theory of Non-Uniform Gases* (Cambridge University Press, Cambridge, 1991).

[48] H. van Beijeren and M. H. Ernst, Physica **68**, 437 (1973).

[49] R. F Snider, G. W. Wei, and J. G. Muga, J. Chem. Phys. **105**, 3066 (1996).

[50] H. M. Antia, Astrophys. J. Suppl. Ser. **84**, 101 (1993).

[51] T. Fukushima, Appl. Math. Comput. **259**, 708 (2015).

[52] Fits of the form $4\pi e^2 n_e/[T^p + (\frac{2}{3}E_F)^p]^{1/p}$ to the TF screening length yield relative errors below 2.5% with $p = 2$, which has maximal error near $T = E_F$. An improvement to relative errors below 1.1% is obtained by choosing $p = 9/5$.

[53] M. S. Murillo, High Energy Density Phys. **4**, 49 (2008).

[54] L. G. Stanton and M. S. Murillo, Phys. Rev. E **91**, 033104 (2015).

[55] S. Ogata, H. Iyetomi, S. Ichimaru, and H. M. Van Horn, Phys. Rev. E **48**, 1344 (1993).

[56] M. M. Marinak *et al.*, Phys. Plasmas **8**, 2275 (2001).

[57] J. D. Ramshaw, J. Non-Equilib. Thermodyn. **18**, 121 (1993).

[58] D. Livescu, Philos. Trans. R. Soc. London A **371**, 20120185 (2013).

[59] G. K. Batchelor, *An Introduction to Fluid Dynamics* (Cambridge University Press, Cambridge, 2000).

[60] K. Molvig, E. L. Vold, E. S. Dodd, and S. C. Wilks, Phys. Rev. Lett. **113**, 145001 (2014).

[61] B. L. Holian, M. Mareschal, and R. Ravelo, Phys. Rev. E **83**, 026703 (2011).

[62] H. Ohta and S. Hamaguchi, Phys. Plasmas **7**, 4506 (2000).

[63] D. B. Boercker and E. L. Pollock, Phys. Rev. A **36**, 1779 (1987).

[64] J. P. Hansen, F. Joly, and I. R. McDonald, Physica A **132**, 472 (1985).

[65] Lord Rayleigh, Proc. London Math. Soc. **14**, 170 (1883).

[66] G. I. Taylor, Proc. R. Soc. London Ser. A **201**, 192 (1950).

[67] D. H. Sharp, Physica D **12**, 3 (1984).

[68] T. Wei and D. Livescu, Phys. Rev. E **86**, 046405 (2012).

[69] R. E. Duff, F. H. Harlow, and C. W. Hirt, Phys. Fluids **5**, 417 (1962).

[70] Z. Donko and P. Hartmann, Phys Rev. E **78**, 026408 (2008).

[71] L. V. Zhigilei, Z. Lin, and D. S. Ivanov, J. Phys. Chem. C **113**, 11892 (2009).

[72] J. Lindl, Phys. Plasmas **2**, 3933 (1995).

[73] G. S Fraley, E. J. Linnebur, R. J. Mason, and R. L. Morse, Phys. Fluids **17**, 474 (1974).

[74] M. Chollet *et al.*, J. Synchrotron Radiat. **22**, 503 (2015).

[75] L. Jiang and H.-L. Tsai, J. Heat Transf. **127**, 1167 (2005).

[76] D. S. Ivanov and L. V. Zhigilei, Phys. Rev. B **68**, 064114 (2003).

[77] O. L. Caballero, S. Postnikov, C. J. Horowitz, and M. Prakash, Phys. Rev. C **78**, 045805 (2008).

[78] Z. Donko and P. Hartmann, Phys. Rev. E **69**, 016405 (2004).

[79] D. J. Evans and G. P. Morriss, *Statistical Mechanics of Nonequilibrium Liquids* (Australian National University Press, Canberra, 2007).

[80] A. Marocchino, M. Tzoufras, S. Atzeni, A. Shiavi, P. D. Nicolai, J. Mallet, V. Tikhonchuk, and J.-L. Feugeas, Phys. Plasmas **20**, 022702 (2013).

[81] J. F. Luciani, P. Mora, and J. Virmont, Phys. Rev. Lett. **51**, 1664 (1983).

[82] L. E. Reichl, *A Modern Course in Statistical Physics* (Wiley, New York, 1998).

[83] G. Zwicknagel, C. Toepffer, and P. G. Reinhard, Phys. Rep. **309**, 117 (1999).

[84] M. S. Murillo, J. Weisheit, S. B. Hansen, and M. W. C. Dharma-wardana, Phys. Rev. E **87**, 063113 (2013).

[85] R. P. Feynman, N. Metropolis, and E. Teller, Phys. Rev. **75**, 1561 (1949).

[86] R. M. More, Adv. At. Mol. Phys. **21**, 305 (1985).

[87] C. Muckenfuss, J. Chem. Phys. **59**, 1747 (1973).

[88] C. F. Curtiss, J. Chem. Phys. **49**, 2917 (1968).

[89] L. Bildsten and D. M. Hall, Astrophys. J. **549**, L219 (2001).

[90] P. Chang, L. Bildsten, and P. Arras, Astrophys. J. **723**, 719 (2010).

[91] M. V. Beznogov and D. G. Yakovlev, Phys. Rev. Lett. **111**, 161101 (2013).

[92] J. O. Hirschfelder, R. B. Bird, and E. L. Spotz, Chem. Rev. **44**, 205 (1949).

[93] J. O. Hirschfelder, C. F. Curtiss, and R. B. Bird, *Molecular Theory of Gases and Liquids* (Wiley-Interscience, New York, 1964).

[94] J. M. Burgers, *Flow Equations For Composite Gases* (Academic Press, New York, 1969).

[95] V. M. Zhdanov, *Transport Processes in Multicomponent Plasma* (Taylor & Francis, New York, 2002).

[96] See S. Chapman and T. G. Cowling, *The Mathematical Theory of Non-Uniform Gases* (Ref. [47]), Chap. 18, on mixtures.